Development of a New Dark Field Imaging Concept and Investigation of Prototype Performance

Dissertation
zur Erlangung des akademischen Grades

Doktoringenieurin
(Dr.-Ing.)

von Xiaolei Yan, M.Sc.
geb. am 15.11.1984 in Jin Chang, China
genehmigt durch die Fakultät für Elektrotechnik und Informationstechnik
der Otto-von-Guericke-Universität Magdeburg

Gutachter: Prof. Dr. Christoph Hoeschen, Otto-von-Guericke-Universität Magdeburg
apl.-Prof. Dr. habil. Thilo Michel, Friedrich-Alexander-Universität Erlangen-Nürnberg
Prof. Dr. Florian Grüner, Universität Hamburg

Promotionskolloquium am 21.10.2025

Abstract

X-ray interferometry has emerged as a powerful imaging technique, offering capabilities beyond conventional absorption-based methods. By providing access to phase contrast and dark-field signals, it's crucial for visualizing weakly absorbing microstructures at the micro-scale for diagnosis and even nano-scale for material inspection. However, this technique traditionally relies on large-scale facilities like synchrotrons or the use of additional source gratings, both of which hinder its feasibility in clinical and laboratory settings. This PhD thesis addresses these limitations by presenting the development and comprehensive evaluation of a novel compact X-ray interferometry-based dark-field (DF) imaging concept. This system integrates a microfocus X-ray tube, an energy-resolved, pixellated photon-counting detector, and a Talbot grating interferometer. The core objective is to demonstrate the system's feasibility and functionality, including its data processing and image optimization, with the ultimate goal of enabling early-stage disease diagnosis in clinical applications like mammography and infectious lung disease.

This research specifically focuses on the dark-field modality to achieve simplified and compact X-ray interferometry. This approach, while simultaneously acquiring phase contrast images, crucially departs from relying on large-scale synchrotrons or additional source gratings by utilizing a partially spatially coherent X-ray source.

A primary goal of this work is to optimize experimental protocols for high image visibility. This involves understanding the critical interplay between data processing and system settings, including detector positioning and X-ray tube voltage. Furthermore, this PhD work also concentrated on optimizing dark-field (DF) image reconstruction, identifying an optimal strategy for Fourier series coefficient generation.

Significantly, the study demonstrates that precise energy matching of the bin of interest (BoI) isn't always essential, which provides valuable flexibility, especially under conditions of limited photon flux. Two complementary optimization approaches (detailed in Chapter 5) are shown to significantly enhance DF image quality by improving scattering feature visibility and reducing noise.

Finally, a viable strategy for further enhancing phase contrast images is proposed. This involves combining goodness-of-fit thresholding to filter poorly fitted pixels with subsequent interpolation to mitigate inherent beam coherence limitations.

This PhD work successfully demonstrates the feasibility and optimized performance of a compact X-ray interferometry system, paving the way towards practical clinical and laboratory deployment.

Zusammenfassung

Die Röntgeninterferometrie hat sich als leistungsstarkes Bildgebungsverfahren etabliert und bietet Möglichkeiten, die über herkömmliche absorptionsbasierte Methoden hinausgehen. Durch den Zugriff auf Phasenkontrast- und Dunkelfeldsignale ist sie entscheidend für die Visualisierung schwach absorbierender Mikrostrukturen im Mikromassstab für die Diagnostik und sogar im Nanomassstab für die Materialprüfung. Diese Technik erfordert jedoch traditionell Grossanlagen wie Synchrotrons oder den Einsatz zusätzlicher Quellengitter, was ihre Durchführbarkeit im klinischen und Laborbereich einschränkt. Diese Dissertation geht auf diese Einschränkungen ein, indem sie die Entwicklung und umfassende Evaluierung eines neuartigen, kompakten Dunkelfeld-Bildgebungskonzepts auf Basis der Röntgeninterferometrie präsentiert. Dieses System integriert eine Mikrofokus-Röntgenröhre, einen energieaufgelösten, pixelierten Photonenzähldetektor und ein Talbot-Gitterinterferometer. Kernziel ist der Nachweis der Machbarkeit und Funktionalität des Systems, einschliesslich seiner Datenverarbeitung und Bildoptimierung, mit dem Ziel, die Frühdiagnose von Krankheiten in klinischen Anwendungen wie der Mammographie und bei infektiösen Lungenerkrankungen zu ermöglichen.

Diese Forschung konzentriert sich speziell auf die Dunkelfeld-Modalität zur Erzielung einer vereinfachten und kompakten Röntg-

geninterferometrie. Dieser Ansatz, der gleichzeitig Phasenkontrastbilder erfasst, verzichtet entscheidend auf grossflächige Synchrotrons oder zusätzliche Quellengitter und nutzt stattdessen eine partiell räumlich kohärente Röntgenquelle.

Ein Hauptziel dieser Arbeit ist die Optimierung experimenteller Protokolle für eine hohe Bildsichtbarkeit. Dies beinhaltet das Verständnis des kritischen Zusammenspiels zwischen Datenverarbeitung und Systemeinstellungen, einschliesslich Detektorpositionierung und Röntgenröhrenspannung. Darüber hinaus konzentrierte sich diese Doktorarbeit auf die Optimierung der Dunkelfeld-Bildrekonstruktion (DF) und die Identifizierung einer optimalen Strategie zur Generierung von Fourierreihenkoeffizienten.

Die Studie zeigt insbesondere, dass eine präzise Energieanpassung des Bin of Interest (BoI) nicht immer zwingend erforderlich ist, was wertvolle Flexibilität bietet, insbesondere unter Bedingungen begrenzten Photonenflusses. Zwei komplementäre Optimierungsansätze (detailliert in Kapitel 5) verbessern die DF-Bildqualität deutlich, indem sie die Sichtbarkeit von Streumerkmalen verbessern und Rauschen reduzieren.

Abschliessend wird eine praktikable Strategie zur weiteren Verbesserung der Phasenkontrastbilder vorgeschlagen. Dabei wird die Anpassungsgüteschwellenwertbildung zur Filterung schlecht angepasster Pixel mit anschliessender Interpolation kombiniert, um inhärente Einschränkungen der Strahlkohärenz zu minimieren.

Diese Doktorarbeit demonstriert erfolgreich die Machbarkeit und optimierte Leistung eines kompakten Röntgeninterferometriesys-

tems und ebnet damit den Weg für den praktischen Einsatz in Klinik und Labor.

Contents

List of Abbreviations

All-Bins All (full) spectrum of photon energy bins

Att Attenuation imaging

BoI Bin of interest

COPD Chronic Obstructive Pulmonary Disease

CT Computed tomography

DF Dark field

DFI Dark-field imaging

DFCT Dark-field CT

Eq-I Equation 3.1

Eq-II Equation 5.2

GoF Goodness of Fitting

IR Ionizing radiation

PPBC Propagation-based phase contra

PC Phase contrast

PCI Phase contrast imaging

SAS Small angle scattering

TD Talbot distance

frTD Fractional Talbot distance

List of Symbols

f_m	The m^{th} order of fractional Talbot distance
Z	Atomic number
Z_T	Talbot distance
p_1	Period of phase grating
p_2	Period of analyzer grating
p_t	Period of lateral intensity profile of interference pattern

1

Introduction

This thesis presents the development and evaluation of a novel X-ray interferometry-based dark-field (DF) imaging concept for a compact, high-resolution system. The core objective is to demonstrate the feasibility and functionality of this proposed imaging concept, including its data processing pipeline and defined image optimization. This work ultimately aims to enable such a system for early-stage disease diagnosis in clinical applications, particularly in areas like mammography and infectious lung disease.

1.1 Motivation and Background

Since their discovery, X-rays have revolutionized non-invasive medical imaging for both diagnosis and therapy. This advancement largely stems from our understanding of ionizing radiation (IR) and our ability to exploit how X-rays penetrate the body and interact with tissues and bones to create varying levels of image contrast. Historically, absorption contrast, which relies on differences in X-ray absorption by human tissues, has been the most prevalent imaging mechanism [1–4]. However, this method's utility for soft tissues is limited due to their similar atomic numbers and not far-off ab-

sorption difference, resulting in poor image contrast. Consequently, alternative contrast mechanismssuch as X-ray scattering and phase shifts of the X-ray wavefrontare gaining prominence. Offering high sensitivity to subtle structural variations and excellent edge differentiation, these methods provide valuable complementary diagnostic information, particularly for detecting micro-scaled abnormalities, and are promising tools for early-stage disease detection in clinical applications [5–16].

While these advanced radiation-based techniques hold great promise, the broader landscape of non-invasive imaging also includes non-ionizing modalities like magnetic resonance imaging (MRI) and ultrasound. MRI leverages the magnetic properties of hydrogen protons, exciting them with radio frequency pulses and detecting the energy they emit as they realign with the main magnetic field. Ultrasound, also known as sonography, generates images by transmitting high-frequency sound waves into the body and detecting the echoes reflected from tissues. These echoes are then reconstructed into visual signals that enable the differentiation of tissue abnormalities based on their distinct acoustic properties. Though these methods often provide significantly higher soft-tissue contrast, they come with their limitations, particularly in terms of image resolution. For instance, they can suffer from relatively low spatial resolution in larger anatomical areas, such as the thoracic and abdominal regions, or necessitate a compromise in signal-to-noise ratio for improved resolution. Specifically, owing to long acquisition procedures and high sensitivity to motion artifacts, MRI

application for investigating pulmonary or respiratory conditions remains challenging and is frequently recommended only as an alternative for high-risk patients susceptible to repeated or excessive radiation exposure [17–19].

While conventional diagnostic radiography remains a primary diagnostic tool, Computed Tomography (CT) was developed to further enhance IR imaging quality. Compared to MRI and ultrasound, CT offers higher spatial resolution for larger anatomical scales and provides a direct physical representation of scanned materials [20]. In principle, CT images are essentially maps of X-ray linear attenuation coefficients. The primary mechanisms of attenuation of X-rays in the diagnostic energy range (20 - 150 keV, photo-electric effect and Compton scattering) depend strongly on the atomic number (Z) and electron density (ρ_e) of the material. While CT effectively differentiates tissues with significant atomic-number disparities (e.g., bone versus soft tissue), its absorption-based mechanism yields inherently low soft tissue contrast given their similar atomic numbers. To overcome this, radio-opaque contrast media, such as iodine or barium, are frequently utilized to modify the attenuation characteristics of soft tissues and improve their visualization. Beyond patient tolerance and concerns regarding elimination, contrast agents pose inherent technical challenges for CT image enhancement, notably their limited selective uptake. This is because, even with contrast agents, the underlying physics for CT image contrast still relies on the fundamental differences in atomic number and electron density for their corresponding attenuation effect. Beyond this challenge

in soft tissue contrast, a broader limitation of absorption-based X-ray imaging concerns dose optimization: the photon absorption cross-section for X-rays drops significantly with increasing energies, which restricts the application of high-energy X-rays for dose reduction [21].

To address these persistent challenges and unlock new possibilities for soft tissue imaging, other IR-based imaging contrast mechanisms have been explored. A key focus has been on exploiting the wave properties of X-rays, specifically the wavefront distortion. The resulting differentiated phase information generates an image signal known as phase contrast imaging (PCI), which offers excellent contrast for distinguishing soft tissue. The principle of X-ray phase contrast imaging relies on the refraction and disturbance of wavefront, inducing usable signals with inherently greater contrast than traditional absorption for certain scenarios, especially those involving subtle density variations and weak absorptions in soft tissues [6, 22, 23]. Crucially, the phase shift of X-rays scales linearly with the electron density of the interacting material and X-ray wavelength. This linearity contrasts sharply with the third-power wavelength dependency of the absorption coefficient, thereby allowing for improved soft tissue contrast while also facilitating dose optimization through the use of higher energy X-rays [6, 24–26].

Generally, there are three primary experimental approaches to phase contrast imaging in the X-ray regime: propagation-based phase contrast (PBPC), crystal interferometry, and grating interferometry. Propagation-based phase contrast imaging, easily

compatible with a conventional polychromatic X-ray tube, relies on free-space propagation over a sufficient distance to magnify wavefront distortions. While conceptually simple, its application often requires significant operating space, which can be a practical limitation, especially in clinical settings [6, 22, 23, 27–29]. While coherence enhancement approaches using liquid-anode metal jet X-ray tubes - that allow partial improvement in temporal coherence using target K-Shell emission lines and spatial coherence length through small focal spots - have demonstrated propagation-based X-ray phase contrast imaging in lab settings [30–32]. However the field of view remains limited to a few millimeters due to narrow beam aperture, limiting applications to small size-scale. Furthermore, crystal interferometers critically require rigorous mechanical stability and extremely precise optical alignment to provide a trustworthy baseline for extracting phase difference between with and without an object. This also presents a significant limitation for widespread clinical application [6]. In contrast, grating-based X-ray interferometric techniques offer a notable advantage with their decreased setup alignment requirements. These techniques directly exploit the wave-like characteristics of X-rays by employing a phase grating and an analyzer grating to induce and analyze phase changes, thereby generating contrast.

X-ray grating interferometry has proven to be a promising advanced medical imaging technique in recent years due to its unique capability of simultaneously acquiring attenuation, phase contrast (PC), and dark-field (DF) images. This allows for a direct, voxel-

based comparison of the absorption, refraction, and scattering properties of X-rays within the scanned material [28, 33, 34]. These combined characteristicsthe simultaneous acquisition of multiple image modalities, high resolution, and low doseoffer significant potential for medical impact through improved diagnostic capabilities.

Concurrently acquired through X-ray interferometry, dark-field imaging offers exceptional sensitivity to microstructural changes, enabling the detection of structural abnormalities at the nanoscale [35]. In medical applications, DF imaging has shown particular promise in areas such as breast calcification detection and lung disease diagnosis [7–16, 36]. For instance, Willer et al. demonstrated the clinical potential of dark-field chest imaging in Chronic Obstructive Pulmonary Disease (COPD) patients, revealing superior sensitivity to lung parenchyma microstructural changes with reduced radiation dose compared to CT [16]. Similarly, Gao et al. showed improved lung cancer nodule detectability in mice using dark-field CT (DFCT) [37].

However, achieving sufficient beam coherence for X-ray interferometry remains a significant challenge, often requiring synchrotron sources or a Talbot-Lau concept (adding a third grating right behind the X-ray tube), leading to large-scale experimental setups. Even compact quasi-monochromatic beam setups, such as the Munich Compact Light Source (MuCLS) for high special resolution radiography, can occupy substantial laboratory space up to 16 meters [38–40]. While source gratings coupled with broad-focus X-ray tubes offer spatial coherence, they significantly reduce photon

flux, impacting image quality and scan time. Another method, like dual-phase-grating interferometry, addresses flux degradation, however, its reliance on propagation distance results in large setups and maintains the environmental sensitivity of phase contrast imaging, demanding critical experimental stability [41–46].

Furthermore, despite the extensive research on phase contrast imaging using X-ray interferometry, dark-field imaging, with its high-resolution microstructural sensitivity, seems to be an equally promising approach. Notably, there is a lack of research focusing on dark-field imaging through X-ray interferometry without increasing system complexity. Benchtop-capable interferometric systems, fitting laboratory length scales and in vivo scan-time scales, are therefore critical in order to broaden accessibility beyond synchrotron facilities and overcome resource-intensive apparatus, making X-ray interferometry-based dark-field imaging feasible in standard research settings.

This thesis aims to address these gaps, specifically overcoming flux losses from source grating-based interferometric configurations, by developing and evaluating a novel, compact benchtop X-ray interferometry system optimized for dark-field imaging.

1.2 Objectives and Limitations

This PhD work aims to develop and evaluate a novel, compact X-ray interferometry imaging system for potential medical applications. The system that is described within this thesis incorporates a microfocus X-ray tube and an energy-resolved, pixellated photon-

counting detector, in addition to a Talbot grating interferometer, to acquire and optimize dark-field images.

To establish the technical feasibility and functionality of this system and its associated methods, the following sub-objectives were pursued: preliminary feasibility assessment of dark-field imaging using a non-biological object (screw with fine thread line structure, used to generate small-angle scattering); development of an experimental protocol for the proposed setup; implementation of optimization methods for reconstructed dark-field images; and exploration of optimization on phase contrast images. While the long-term goal is a medical application, this work primarily focuses on the technical development and evaluation of the imaging system.

The primary limitations of this study stem from the microfocus X-ray tube's insufficient beam coherence and the potential for noisy results due to low flux. Additionally, challenges in achieving precise alignment for X-ray interference were anticipated. In addition to these theoretical constraints, practical limitations within the X-ray laboratory impacted the experimental process. These challenges arose from:

Using a non-biological object (a screw with a fine thread line structure designed for small-angle scattering) for technical testing, instead of biological samples.

The necessity of device repairs and ongoing maintenance.

Therefore, this research primarily focuses on the technical development and feasibility of the imaging system, with medical applications considered for future studies.

1.3 Definitions of Key Terms

X-ray interferometry: Similar to optical interferometry, X-ray interferometry utilizes the wave properties of X-rays to split and recombine beams, resulting in diffraction and interference patterns. X-ray optical elements, including crystals and gratings, can manipulate X-ray beams based on principles such as Bragg diffraction and grating diffraction, allowing for controlled interference and focusing.

X-ray grating interferometry: This technique employs periodic structures, such as gratings, to split and recombine X-ray beams. Grating interferometry, which is central to this PhD work, will be discussed in detail in Chapter 2.

X-ray dark-field imaging: In X-ray interferometry, dark-field imaging quantifies the ultra-small-angle scattering properties of a sample. This is achieved by analyzing the visibility reduction of the interference pattern caused by the sample's microscopic structures. The resulting image represents the spatial distribution of scattering power, where brighter regions correspond to areas with higher scattering intensity.

Dark-field microscopy: Unlike X-ray dark-field imaging, optical dark-field microscopy utilizes a specialized condenser or objective lens to block the direct, unscattered light from reaching the detector. This results in only the light scattered by the specimen, particularly at edges and interfaces, being collected. Consequently, the image displays a dark background with bright features, highlighting the object's boundaries and fine details.

Phase contrast imaging: Two primary techniques are employed for generating phase contrast images: propagation-based and grating interferometry-based.

Propagation-based phase contrast imaging: This method relies on the free-space propagation of X-rays after interaction with a sample. The phase shifts induced by the sample's refractive index variations are converted into detectable intensity modulations at a downstream detector. This conversion occurs due to Fresnel diffraction, which is highly sensitive to the propagation distance and the spatial coherence of the X-ray beam. Consequently, this technique is susceptible to variations in experimental conditions, including sample-detector alignment and temperature-induced dimensional changes, which can affect the propagation distance and beam stability.

1.4 Outline

The following is a brief overview of the thesis structure. Chapter 1 provides a context for this research by reviewing the state-of-the-art in X-ray medical imaging, focusing on interferometry-based systems, and outlining the study's objectives and limitations. Chapter 2 details the fundamental principles of X-ray interferometry, specifically imaging signal extraction. Chapters 3, 4, and 5 present the core contributions of this work, focusing on the design, feasibility, and optimization of the proposed system. Specifically, Chapter 3 introduces the imaging hypothesis and system concept design with initial experimental results. Chapter 4 examines the feasibility of

the designed setup. Chapter 5 focuses on dark-field image analysis and optimization. Chapter 6 concludes the thesis by summarizing the findings and suggesting future research directions.

2

Theoretical Background

This chapter begins with a brief description of the basic mechanisms of X-ray interaction with matter in section 2.1, followed by an introduction of X-ray interferometry imaging techniques in section 2.2. For an in-depth exploration of theoretical principles underlying grating-based techniques, including beam divergence and coherence, fringe analysis methods, and other related aspects, readers are directed to Chapters 1 and 2 of S. Rutishauser's doctoral thesis 'X-ray grating interferometry for imaging and metrology' [47]. This benefits effective reading for experts in the field while offering a comprehensive physics foundation.

2.1 Interactions Between X-rays and Matter

The interactions between X-rays and matter are fundamental to various applications, such as imaging, spectroscopy, material analysis, and so on. These interactions occur when X-rays pass through or encounter matter and can be categorized into several key phenomena, as shown in Figure 2.1 [48]:

Photoelectric effect: An X-ray photon transfers all its energy to an inner-shell electron and ejects the electron from the atom

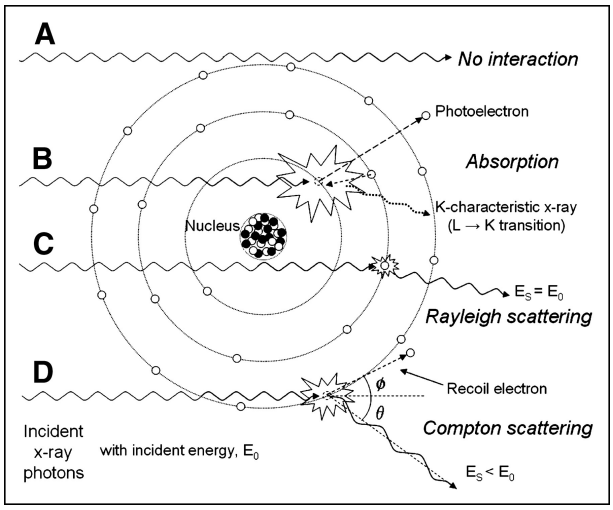

Figure 2.1: Illustrative of X-ray interactions. (A) Unattenuated beam; (B) Photoelectric absorption; (C) Rayleigh scattering; (D) Compton scattering.Figure resourced from [48]

(photoelectron), the so-called ionization of the atom. Consequently, the electron vacancy is filled by an outer-shell electron, releasing energy as a characteristic X-ray or Auger electron. The photoelectron effect dominates at lower X-ray energies and in materials with high atomic numbers. It forms the basis for techniques like X-ray absorption or fluorescence (XRF).

Compton scattering: An X-ray photon collides with an out-shell electron, transferring some of its energy to the electron and scattering to a new direction with reduced energy. This effect is more prominent at higher X-ray photon energy, contributing to radiation scattering and causing a degraded image quality.

Coherent scattering (Rayleigh scattering): An X-ray photon interacts with an atom, causing the entire atom to vibrate and re-emit an X-ray photon with the same energy but in a different direction. There is no energy transfer in this effect besides a change in the direction of the X-ray photon. This effect is minimal and has little impact on imaging or radiation therapy.

Pair production: An X-ray photon interacts with the nucleus of an atom, converting its energy into an electron-positron pair. The creation of two particles, an electron and a positron, can further interact with the matter. This effect occurs only at high X-ray energies and is relevant in high-energy radiation therapy.

2.2 Grating-Based X-ray Interferometry

Although X-ray interactions with matter primarily yield absorption-based images, the wave nature of X-rays causes wavefront distortions upon passing through a subject, due to variations in the phase of the wave. By introducing a grating into the beam path, X-ray waves are forced to interfere, producing an interference pattern. X-ray interferometry then measures the intensity of this pattern to quantify the distortions (phase variations) and generate imaging signals. Phase variations can also be measured by increasing the X-ray propagation distance, also known as propagation-based phase contrast imaging, a technique outside the scope of this thesis but detailed in S. W. Wilkins et al.'s and A. Snigirev et al.'s papers [49, 50]. The following subsections discuss two key components of X-ray interferometry techniques: 1). Talbot effect; 2). Phase-stepping.

2.2.1 Talbot Effect

Talbot effect, a characteristic near-field diffraction (Fresnel Diffraction) phenomenon, manifests the wave field when a coherent wave, such as a monochromatic beam or plane wave, passes through a grating with a period comparable to the incident wavelength [51–54].

The resulting interference pattern, known as the Talbot carpet, is directly observable in the visible light regime. In contrast, visualization of the Talbot effect for X-rays relies on simulations derived from mathematical models implemented using software packages like MATLAB or Wolfram Mathematica.

In this thesis, the paraxial Fresnel diffraction wave field is simulated using MATLAB. Figure 2.2 shows simulated Talbot interference patterns generated by plane wave illumination after passing through: a) a $\pi/2$ phase-shift grating, and b) a π phase-shift grating. While Talbot patterns can be generated by both absorption and phase gratings, phase gratings are preferred in X-ray interferometry imaging techniques due to their superior photon flux efficiency. Unlike absorption gratings, which significantly attenuate the X-ray beam, phase gratings primarily shift the wavefront's phase, allowing a much higher proportion of photons to contribute to the interference pattern. Specifically, phase gratings are designed to induce a controlled phase shift in the incident wave while minimizing absorption. The design energy of a phase grating, determined by the height h of its bars and the atomic number Z of its material, is thus defined as the specific wavelength (or photon energy) intended to achieve the desired phase shift [51, 55].

Along the propagation direction, the wave field variations caused by the phase grating manifest as a modulated intensity distribution due to phase differences, forming the Talbot carpet. Maximum and minimum intensity distributions correspond to in-phase and out-phase conditions, respectively. A notable characteristic of Talbot

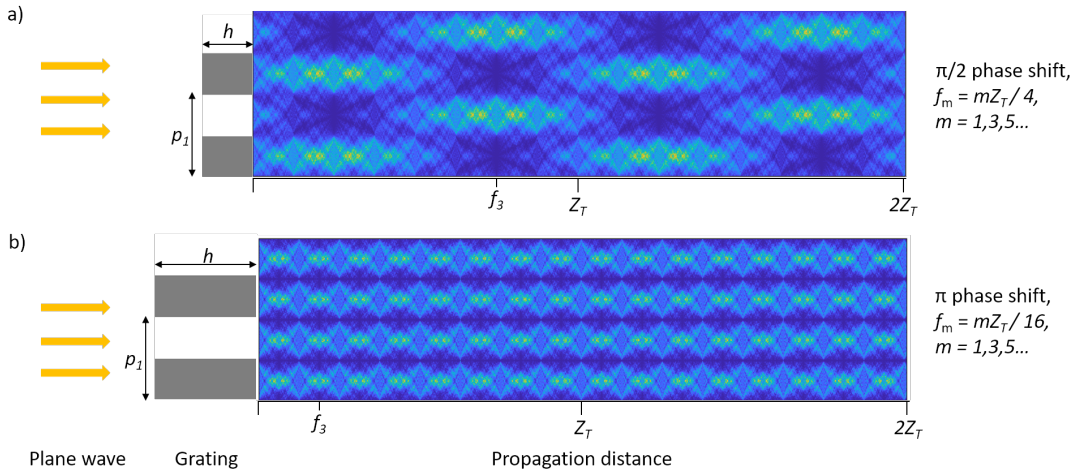

Figure 2.2: Talbot carpets simulated over a propagation distance of 2 Z_T , induced by, a) $\pi/2$ phase-shift grating; b) π phase-shift grating. Maximum intensity modulation, revealing the grating structure, occurs at fractional Talbot distances f_m, with the specific equations for calculating f_m for each phase grating type provided on the right side of the figure.

carpets is the periodic recurrence of this intensity pattern along the propagation direction, with a characteristic Talbot distance (Z_T) given by (The derivation is presented in the Appendix A.1):

$$Z_T = \frac{2p_1^2}{\lambda} \tag{2.1}$$

Here, p_1 is the grating period and λ is the wavelength of the incident beam. The derivation of the paraxial Fresnel approximation and the corresponding Talbot distance is presented in Appendix A. For consistency with the propagation direction z in describing our coordinate system, the Talbot distance is denoted as Z_t in this PhD work, although it is also commonly represented as d_T.

Within one Talbot distance (TD) Z_T, fractional Talbot distance (frTD), is also defined and noted as f_m, indicating positions where the periodic grating structure is revealed as a maximized intensity modulation along the lateral direction. In Figure 2.2, the third

frTD (f_3) is labeled in both Talbot carpets. Noteworthy, in the $\pi/2$ phase-shift Talbot carpet, the period p_t of the interference pattern at f_m equals the grating period p_1 [51–55], which is

$$p_t = p_1 \tag{2.2}$$

Additionally, for every half Talbot distance, the pattern is transversely shifted by half its period ($p_t/2$). In contrary, the interference pattern period in the π phase-shift Talbot carpet is

$$p_t = \frac{p_1}{2} \tag{2.3}$$

without transverse shift along the propagation direction of the pattern.

In principle, both π and $\pi/2$ phase gratings can be used in X-ray interferometry imaging techniques without causing a difference regarding the imaging signal extraction method which is detailed in the next subsection.

2.2.2 Phase-Stepping Method for Extraction of the Imaging Signal

Phase-stepping, also known as phase-scanning, has been developed and utilized over a long period. In 1966, P. Carré made an outstanding contribution to phase-shifting techniques for wave measurements by developing a four-step algorithm robust to phase-shift inaccuracies. This methodology was then significantly advanced by J. H. Bruning et al. in 1974 with their crucial development in digital phase-measuring interferometry, enabling automated, high-

resolution wavefront analysis [56, 57]. As a significant development in recent decades, F. Pfeiffer et al.'s adaptation of the phase-stepping method for the X-ray imaging field enables signal extraction for three imaging modalities within a single procedure: attenuation, phase contrast, and dark-field (also known as visibility contrast) images.

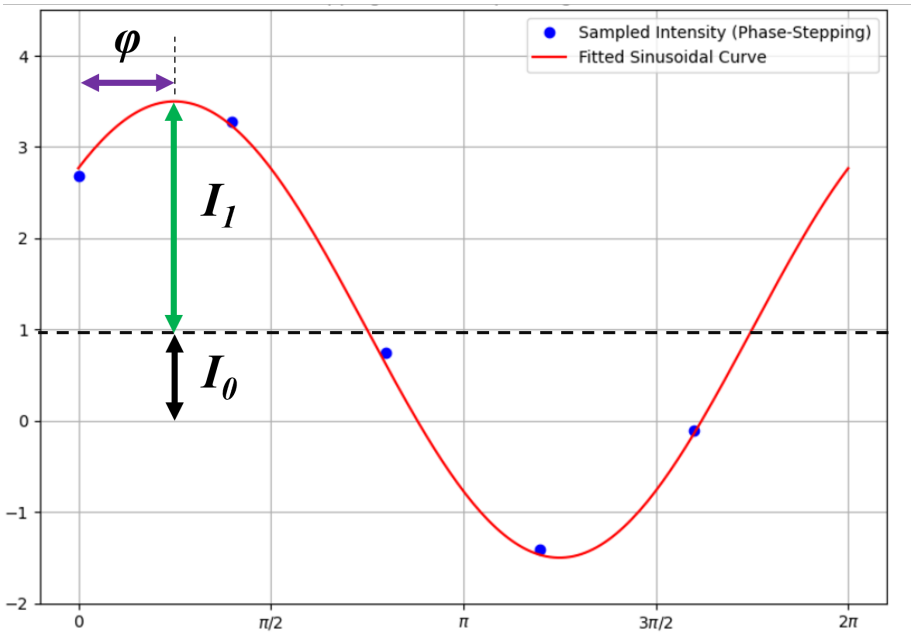

Figure 2.3: Exemplary illustration of Phase-Stepping and signal constituents (coefficients). The sample points represent the measured intensity data points, and the continuous line represents the fitted sine curve. The coefficients are thereby obtained from the fitted curve as shown.

Figure 2.3 shows an exemplary illustration of the phase-stepping method for intensity sampling and extraction of the sine wave coefficients. This figure is obtained by plotting a discretized sine wave in Python, followed by curve fitting for illustration purposes. Based on the principle of wave interference, described by a sinusoidal function and wave superposition, the phase-stepping method involves sampling the intensity of the interference pattern at several discrete positions, seen as the blue dots in Figure 2.3. In addition, since

the brightness of the interference pattern varies periodically, it is only necessary to fit the complete intensity profile over one period to extract the wave information, such as phase, offset, and amplitude, as shown by the red curve and labeled arrows in Figure 2.3. Moreover, the phase-stepping method primarily focuses on lateral intensity sampling, given its reliance on wavefront variations, although the interference pattern shows intensity varying along both the lateral and propagation directions (as seen in Figure 2.2). The mathematical tool of this method is the Fourier series, which allows periodic functions to be represented as a sum of sinusoidal waves with discrete phase shifts. A comprehensive mathematical derivation is provided in chapter 2.4 of the PhD thesis by M. Bench. [58]. The following context will explain the practical approach used for calculating the image signal in the phase-stepping method.

Phase-stepping is often performed with the detector positioned at a fractional Talbot distance. This choice is driven by the maximized intensity modulation observed at these locations, which improves the sensitivity to wavefront distortions induced by the object. After propagating a fractional Talbot distance (frTD) downstream of the phase grating, the intensity of the resulting interference pattern with a period p_t can be represented by a Fourier series in the sinusoidal form as:

$$I(x_g) = \sum_{n=0}^{\infty} I_n \cos\left(2\pi n \frac{x_g}{p_t} - \varphi_n\right) \tag{2.4}$$

Here, x_g represents the stepping position used for sampling the intensity during the phase-stepping procedure, although mathematically it can be treated as a continuous variable. Since the

higher-order terms typically decay rapidly, Eq.(2.4) can often be approximated by the first few terms, and frequently just the first harmonic is considered:

$$I(x_g) \approx I_0 + I_1 \cos\left(2\pi \frac{x_g}{p_t} - \varphi_1\right) \tag{2.5}$$

In this approximation, I_0 represents the average intensity of the modulated wave, which is related to the transmitted intensity through the object. The term φ_1 corresponds to the phase shift induced by the object. Recalling that the Talbot pattern at frTD exhibits a periodic intensity variation (appearing as brightness fringes), the visibility V_f of these fringes is generally defined as:

$$V_f = \frac{I_{max} - I_{min}}{I_{max} + I_{min}} \tag{2.6}$$

By substituting the maximum and minimum intensities from the approximated intensity profile in Eq.(2.5), which occur when the cosine term equals +1 and -1, respectively, the visibility V_f can be expressed as:

$$V_f = \frac{(I_0 + I_1) - (I_0 - I_1)}{(I_0 + I_1) + (I_0 - I_1)} = \frac{2I_1}{2I_0} = \frac{I_1}{I_0} \tag{2.7}$$

Up to this point, we have discussed the spatial intensity distribution of the Talbot pattern at a fractional Talbot distance (frTD) when only a phase grating (meaning without a test sample) is present in the beam path. This can be defined as the reference data, labeled as r. However, when a test sample is additionally introduced into the beam path, the wavefront is no longer system-

atically distributed. By applying phase-stepping in the presence of the test sample, the corresponding wavefront terms discussed previously can also be extracted and are conventionally labeled as s. With the quantitative wavefront information obtained both with and without the sample-induced distortion (i.e., I_0^s vs I_0^r, I_1^s vs I_1^r, and φ_1^s vs φ_1^r), we can now extract image signals characterizing the tested sample:

$$Att = 1 - I_0^s / I_0^r \tag{2.8}$$

$$\Delta\varphi = \varphi_1^s - \varphi_1^r \tag{2.9}$$

$$V = \frac{V_f^s}{V_f^r} = \frac{I_1^s / I_0^s}{I_1^r / I_0^r} = \frac{I_1^s I_0^r}{I_1^r I_0^s} \tag{2.10}$$

In Eq.(2.8), the attenuation image signal (Att) is defined as the complement of the relative transmission, 1-T, where $T = I_0^s / I_0^r$.

2.2.3 Overview of Measurements and Data Processing in Phase-Stepping Method

Building upon the theoretical principles of phase-stepping, in X-ray interferometry, particularly with micrometer-scale grating periods, the continuous sinusoidal intensity profile described by Eq.(2.4) (or the approximated form in Eq.(2.5)) cannot be directly measured. This is because the intensity profile of the pattern along the lateral direction has a period smaller than the detector pixel size. Therefore, the phase-stepping method employs an additional absorption grating (analyzer grating), which has the same period

as the intensity profile and acts as a spatial mask to sample the intensity. Experimentally, the analyzer grating is placed directly before the detector and laterally shifted to sample the intensity pattern $I(x_g)$ at discrete phase steps (x_g). These sampled data points (x_g, $I(x_g)$), as illustrated in Figure 2.3, are subsequently used for curve-fitting to extract the coefficients of the sinusoidal intensity profile.

Following the phase-stepping procedure applied to each detector pixel, the intensity measurements for the i-th pixel at each step x_g form a data set $(x_g, I(x_g))_i$ (in some literature, the coordinates (x, y) are used to represent the pixel matrix index). These data sets are then subjected to curve-fitting to extract the coefficients of the sinusoidal intensity variation for each pixel, resulting in coefficient lists such as $(I_0, I_1, \varphi_1)_i$. It is crucial to recall that this entire process is performed both with and without the testing object to obtain reference and sample data. Subsequently, by using these two data matrices in Equations (2.8), (2.9), and (2.10), the test sample in X-ray interferometry can be mapped and visualized through three primary image modalities represented by the data lists of: attenuation (Att_i), phase shift ($\Delta\varphi_i$), and dark-field (V_i).

Having outlined the basic principles of phase-stepping for X-ray interferometry under the assumption of an ideal monochromatic plane wave, the next chapter will explore more intricate experimental realities, specifically the influence of beam type and the generation of curve-fitting based coefficients.

3

Materials and Methods

This chapter presents the development of the materials and methods employed in this study. It begins by introducing the core idea behind the compact system design and outlining the challenges it aims to address. Subsequently, the chapter details the initial measurements undertaken with the proposed setup and the resulting initial images, which serve as a basis for further investigation and optimization.

3.1 Hypothesis and Challenge of Compact System for Dark-field Imaging

X-ray interferometry imaging techniques typically utilize either a synchrotron with Talbot interferometer (employing only a phase grating and an analyzer grating) or a Talbot-Lau interferometer (besides a phase grating and an analyzer grating, a third gratinga source grating is attached to an X-ray tube). Both configurations aim to provide sufficient beam coherence for interfering X-rays and minimize Talbot pattern imperfections. However, the practical application in clinical and experimental tasks is critically restricted due to either limited access to synchrotron facilities or, the statistical challenges posed by the low flux inherent in Talbot-Lau

interferometry while considering dose constraints.

We hypothesize that the beam coherence for acquiring dark-field images (based on small-angle scattering) is not as strictly required as that for phase contrast images that completely rely on the wave properties of X-rays. Therefore, with the assumption that sufficient beam coherence for interfering X-rays can be provided by a micro-focus X-ray tube without a source grating, this work proposes a compact X-ray interferometry setup for dark-field imaging. The core of this compact system includes: a micro-focus X-ray tube providing partial spatial coherence of the beam; an energy-resolving detector enabling the selection of photons based on energy bins; and Talbot interferometry.

A significant challenge concerning the proposed hypothesis is the potential degradation of the reconstructed image. The partial spatial coherence of the X-ray beam is expected to induce imperfections in the interference pattern, which can lead to additional wavefront aberrations. With the introduced phase-stepping method in Chapter 2, these aberrations may not be fully resolvable and potentially complicate the accurate determination of wavefront parameters, ultimately resulting in inaccuracies in the derived image signals.

To address those challenges, the primary objectives of this PhD work, as detailed in this chapter, are the investigation of the proposed compact system setup for dark field imaging and the development of image optimization solutions. The chapter will proceed with a description of the setup configuration, followed by an outline

of the initial measurement procedure and the initial image results to enable further analysis and optimization in the subsequent chapters.

3.2 Design of a Compact X-ray Interferometry System

3.2.1 Setup Configuration

Continuing with the hypothesis of a compact system, Figure 3.1 illustrates the configuration of the designed setup. A Nova Microfocus System 96000 Series X-ray source was utilized, providing a focal spot size of 14 - 20 μm at maximum voltage and minimum power. The Talbot interferometer employed two gratings, both sourced from MicroWorks GmbH: a phase grating (G1) and an analyzer grating (G2). The phase grating G1 had a period of 2.4 μm, designed to induce a $\pi/2$ phase shift. The analyzer grating G2 had a period of 4.8 μm, chosen to match the magnified interference pattern (magnification factor of 2 due to beam divergence). The inter-grating distance was set to the third fractional Talbot distance.

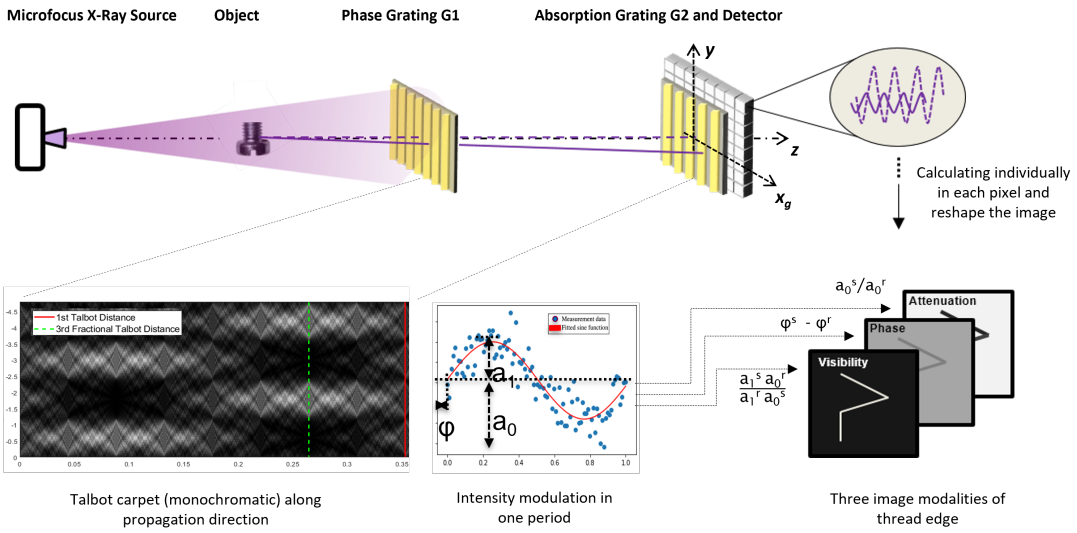

Figure 3.1: Sketch of setup and phase-stepping method (not in scale)

3.2.2 Initial Measurement

In the preliminary experimental study to prove our hypothesis, aluminum screws with 1mm thread pitch, which has micro-structures feasible to generate small-angle scattering distribution, were chosen as our object with the aim of imaging the edge of the thread. X-ray tube voltage of 40 kVp was applied with 2 mm Al and 1 mm Fe filtration to obtain mean energy of about 37.5 keV, therefore satisfying the design energy of phase-grating (37.5 keV). Fourier-transform coefficients of each pixel in the readout region from the Timepix3 detector (Advacam MINIPIX, pixel size of 55μm x 55μm, 256 x 256 pixels array) were computed for revealing thread images in different imaging modes (attenuation contrast, phase contrast, and a visibility contrast i.e. the so-called dark field image).

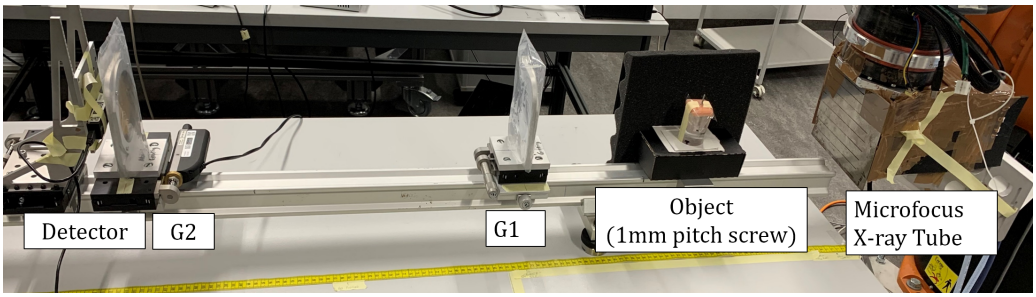

Figure 3.2: Photography of initial experimental setup

To investigate phase-stepping measurements and image computation methods using the curve-fitting methodology for Talbot-interferometer-based imaging, validation experiments were performed using an additional single-pixel Si-PIN detector (MOXTEK, 13 mm^2 active detecting area) with a larger active-area and a better energy resolution than the Timepix3 sensors, and under the same geometrical setup as done for the TimePix3 sensors.

Utilizing the phase-stepping measurement outlined in Chapter 2, both experimental conditions employed the same parameters. The analyzer grating (G2) was translated to 7 discrete positions, with a step size of 0.8 μm. This lateral displacement was achieved using a translation stage driven by a motorized actuator (Newport LTA-HL, minimum incremental motion 0.05 μm, typical accuracy $\pm$1.2 μm).

3.3 Data Processing and Initial Results

The initial experimental data were processed according to the reconstruction method outlined in Subsec. 2.2.2. Curve-fitting was performed to extract Fourier series coefficients of Eq. (2.5), and the fittings were compared between measurements taken with the TimePix3 and Si-PIN detectors, as presented in Figure 3.3.

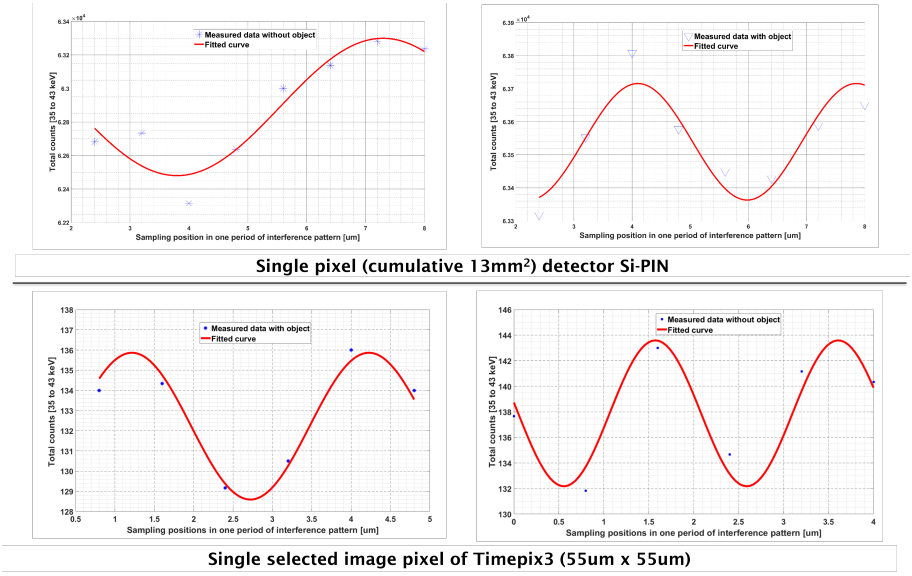

Figure 3.3: Curve fitting of interference pattern in one period with energy-resolved detectors

While data processing revealed some pixels with imperfect fitting, the initial images reconstructed with data acquired using the

TimePix3 detector suggested the potential for successful dark-field and phase contrast imaging, as seen in Figure 3.4.

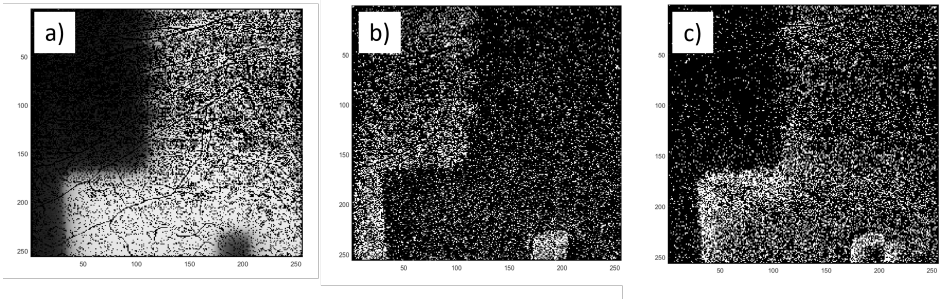

Figure 3.4: Initial reconstruction of three image modalities using Eq. 2.5, showing: a) attenuation; b) phase contrast; c) dark field.

Considering that the actual period of the interference pattern might deviate from the theoretical value, as evidenced by the longer period observed in the top left subplot of Figure 3.3 compared to the other three, Eq.(2.5) was slightly modified for the curve-fitting procedure as follows:

$$I(x_g)^i = I_0^i + I_1^i \cos\left(2\pi \frac{x_g}{p_t^i} - \varphi_1^i\right) \tag{3.1}$$

Here, p_t^i denotes the period determined by the fitting parameters, rather than a fixed constant as in the ideal case. The revised images based on the reconstruction of coefficients of Eq.(3.1) are presented in Figure 3.5

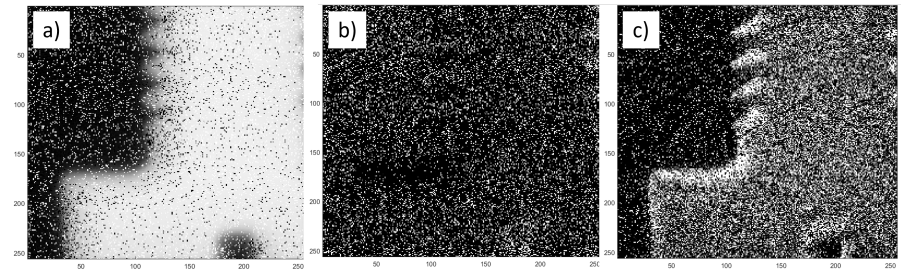

Figure 3.5: Reconstructed three image modalities using coefficients from fitting Eq.(3.1): a) attenuation; b) phase contrast; c) dark field.

The subsequent discussion about the two sets of image results will be presented in Chapter 4 and 5.

4

Investigation of the Compact System Hypothesis

Having established the initial image results, this chapter investigates the feasibility of the proposed compact X-ray interferometry system. It starts with a mathematical model addressing beam chromaticity, followed by a focused investigation of visibility variations arising from beam polychromaticity.

4.1 Mathematical Modeling of the Interference Pattern

While Subsec. 2.2.1 presented a theoretical model of analyzing the interference pattern, beam chromaticity is a crucial factor distinguishing our experimental conditions with interfering X-rays. Based on the superposition principle of waves, the interference pattern generated by a polychromatic beam is mathematically modeled as the summation of wavefields from its elemental wavelengths [59]. Using this model, we can further analyze the intensity modulation of the resulting interference pattern to extract wavefield parameters and quantify the impact of the difference between the theoretical model presented in Chapter 2 and the actual laboratory conditions.

4.1.1 Spectra Measurements

Experiment I.

Initial spectrum investigation experiments (not for imaging)

X-ray source: Nova Microfocus System 96000 Series.

Gratings: MicroWorks ($\pi/2$ Phase grating, g1 = 2.4 μm, design energy 37.5 keV; Analyzer grating, g2 = 4.8 μm).

Filtration options: 1). Fe 1mm + Al 2 mm; 2). W 0.3 mm + Al 2mm; 3). Al 2mm + Fe 1mm + Al 2 mm. Multiple spectra measuring to determine filtration configuration and X-ray tube operation parameters.

Detector: Si-XPIN, high energy-resolution (0.01kev) single-pixel large area (13 mm^2) detector.

Geometry (distance):

G1 - G2: 557 $\pm$ 0.5 mm;

Source - Detector: 1170 $\pm$ 0.5 mm.

Running: 7 positions of G2 within one period; each position 200 seconds, 6 repetitions. The step of 0.08 μm was realize by employing a linear stage driven by a motorized actuator.

Translation Stage: Newport M-436, Manual Linear Stage, 50.8 mm Travel.

Motorized Actuator: Newport LTA-HL, minimum incremental motion 0.05 μm, typical accuracy $\pm$1.2 μm.

Measurements: multiple spectra measuring with and without an object in the beam path to determine filtration configuration and X-ray tube operation parameters.

Results: Within FWHM the effective energy 37.6557 keV can be achieved by running the X-ray tube at 40kvP, 80W, and attaching filters (Fe 1 mm + Al 2 mm) directly in front of the tube window, while an average energy of 33.747 keV over the full spectrum was determined, as shown in Table 4.1.

Experiment II.

Initial experiments (for imaging the object of a metallic screw with 0.5 mm thread line):

The measurements of screw were performed by adapting the operating and geometry parameters from experiment I - spectrum investigation, besides replacing the Si-XPIN by an imaging detector TimePix 3, Advacam MINIPIX. The details are listed as following:

Source: 40kvP, 80W of Nova 96000 Series, 90kV water-cooled Microfocus X-ray Tube

Gratings: MicroWorks ($\pi/2$ Phase grating, g1 = 2.4 μm, design energy 37.5 keV; Analyzer grating, g2 = 4.8 μm)

Detector: TimePix 3, Advacam MINIPIX, pixel size of 55μm x 55μm, 256 x 256 pixels array. Bin width 0.01keV, threshold of detecting level: 5 45 keV.

Geometry: G1-G2 55.77cm; Source - Detector 1170mm

Parameters of Phase-scanning Procedure:

- Scanning Grating (G2): 7 positions

- Step Increment: 0.8 μm

- Acquisition Time per Position: 200 seconds Repetitions per Position: 6

Experiment III.

Spectrum testing of adjusted X-ray tube voltage:

The only experimental parameter varied between Measurement I and Measurement II was the X-ray tube voltage, increased by a small increment (parameters in Table 4.1). This adjustment aimed to achieve an effective energy of the Bin of Interest (BoI) aligned with the phase grating's design energy, while keeping the total count statistics above 75%. The details are:

- Source: 43 kvP, 80 W of Nova 96000 Series, 90kV water-cooled Microfocus X-ray Tube

- Gratings: MicroWorks ($\pi/2$ Phase grating, g1 = 2.4 μm, design energy 37.5 keV; Analyzer grating, g2 = 4.8 μm)

- Detector: TimePix 3, Advacam MINIPIX, pixel size 55μm x 55μm, 256 x 256 pixels array. Bin width 0. 1keV, threshold of detecting level: 5 45 keV.

- Geometry: G1-G2 55.77cm; Source - Detector 1170mm

4.1.2 Photon Energy Spectrum Investigation

To understand the influence of photon energy distribution on the Fourier series coefficients acquired from the fitted intensity profile at the fractional Talbot distance (frTD), we investigated the spectra of the laboratory micro-focus X-ray tube, as detailed in Section 4.1.1. These spectra, acquired under three measurement settings (main operating parameters in Tab. 4.1) and shown in Figure 4.1, were analyzed to determine the wavelength elements of the polychromatic beam. The detailed experimental settings for these three measurements are presented in the Section 4.1.1. The beam

configuration (re-binned photon energy probability distribution) from Measurement II (imaging experiment) was then used in the mathematical model to generate the interference pattern with a polychromatic beam, as detailed in Subsec. 4.1.3 and illustrated in Figures 4.4 and 4.5.

Table 4.1: Spectrum investigation based on three measurements setting.

Measurement	I	II	III
Detector	Si-XPIN	TimePix3	TimePix3
Energy resolution (keV)	0.009	0.01	0.1
Tube voltage (kVp)	40	40	43
$\overline{E}$ of full spectrum (keV)	33.747	33.7784	36.4521
BoI range (keV)	35.56 - 43.12	34.797 - 43.270	31.90 - 42.90
$\overline{E}$ of BoI (keV)	37.6557	37.6651	37.5483

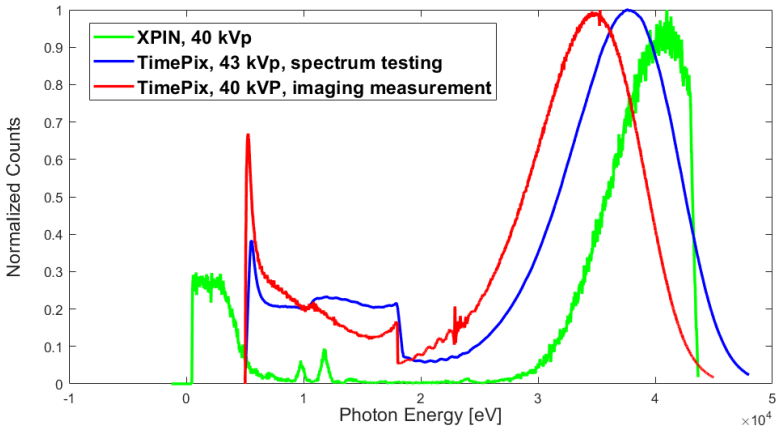

Figure 4.1: Spectrum plots of Microfocus X-ray tube operated in three distinct experiments

In Figure 4.1, the spectra obtained from the TimePix 3 (red) and the XPIN high-energy resolution photon counting detector (green) exhibited notable differences, even under identical X-ray tube operating parameters. Specifically, the XPIN data showed a peak shift towards higher energies. This discrepancy could be attributed to differences in energy resolution between the detectors, or potentially to manually operated miscalibration in the detection

channel setting of the XPIN detector software. The blue spectrum was selected to ensure its effective energy matched the design energy of the phase grating employed in our setup, while maintaining sufficient counts within the Bin of Interest (BoI) (75% of the total). Subsec. 4.1.2 provides a more in-depth discussion regarding the spectra of the three measurements.

Following the initial imaging experiment (Measurement II in Tab. 4.1), the red spectrum outlined in Figure 4.1 was transformed into a probability distribution (histogram), as illustrated in Figure 4.2. Due to memory constraints during the computation of the interference pattern within the Matlab platform, this histogram was then re-binned into 40 photon energy bins (Figure 4.3). Subsequently, the pink range of this re-binned histogram, comprising 20 photon energy bins, was successfully employed to simulate a weighted interference pattern for polychromatic incident beams.

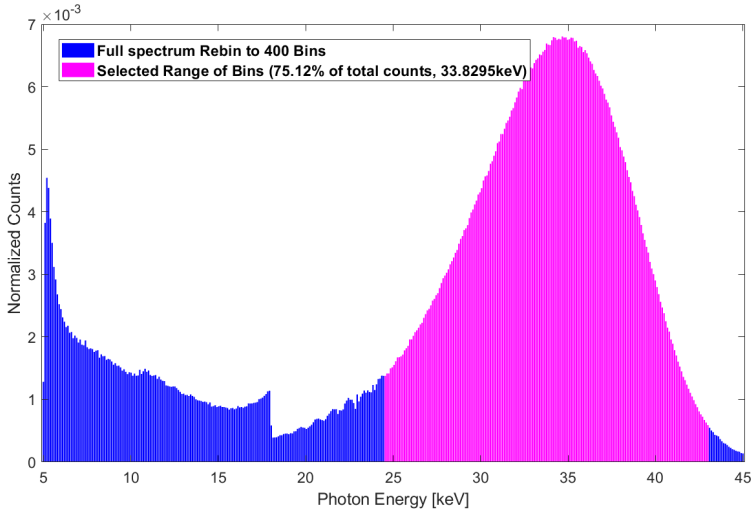

Figure 4.2: Histogram of spectrum re-binned from 4000 to 400 bins, reference data of screw imaging measurements

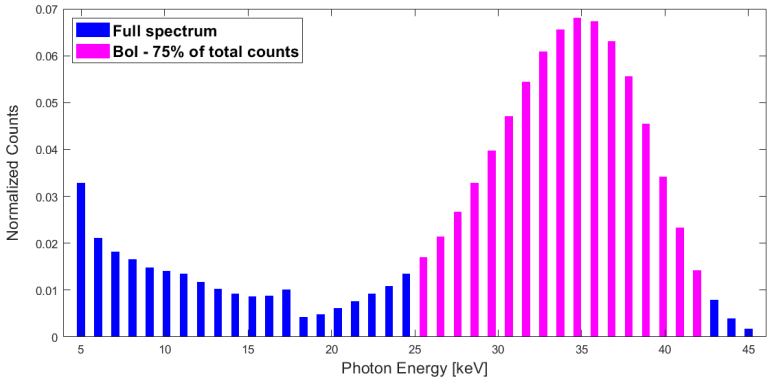

Figure 4.3: Histogram of spectrum re-binned from 4000 to 40 bins, reference data of screw imaging measurements

4.1.3 Talbot Carpet Simulation - Influence of Beam Configuration

The beam configuration in this PhD work, defined as the photon energy probability distribution determined in the previous subsection's spectra investigation, leads to the generation of different Talbot carpets based on various beam configurations.

Figure 4.4 displays three simulated interference patterns generated under different incident beam conditions: a) a monochromatic beam at 37.5 keV (matching the phase grating's design energy); b) a uniformly distributed photon energy spectrum; and c) a photon energy distribution weighted to reflect the experimental setup. A white dashed line in each pattern indicates the third fractional Talbot distance, calculated using the effective energy. It is evident that, along the propagation, the superposition of interference patterns in b) and c) results in blurring with a loss of maximum intensity modulation, even at the fractional Talbot distance. This intensity reduction worsens from b) to c) as the wavefield sum is varied from an equally distributed probability of photon energy to a weighted

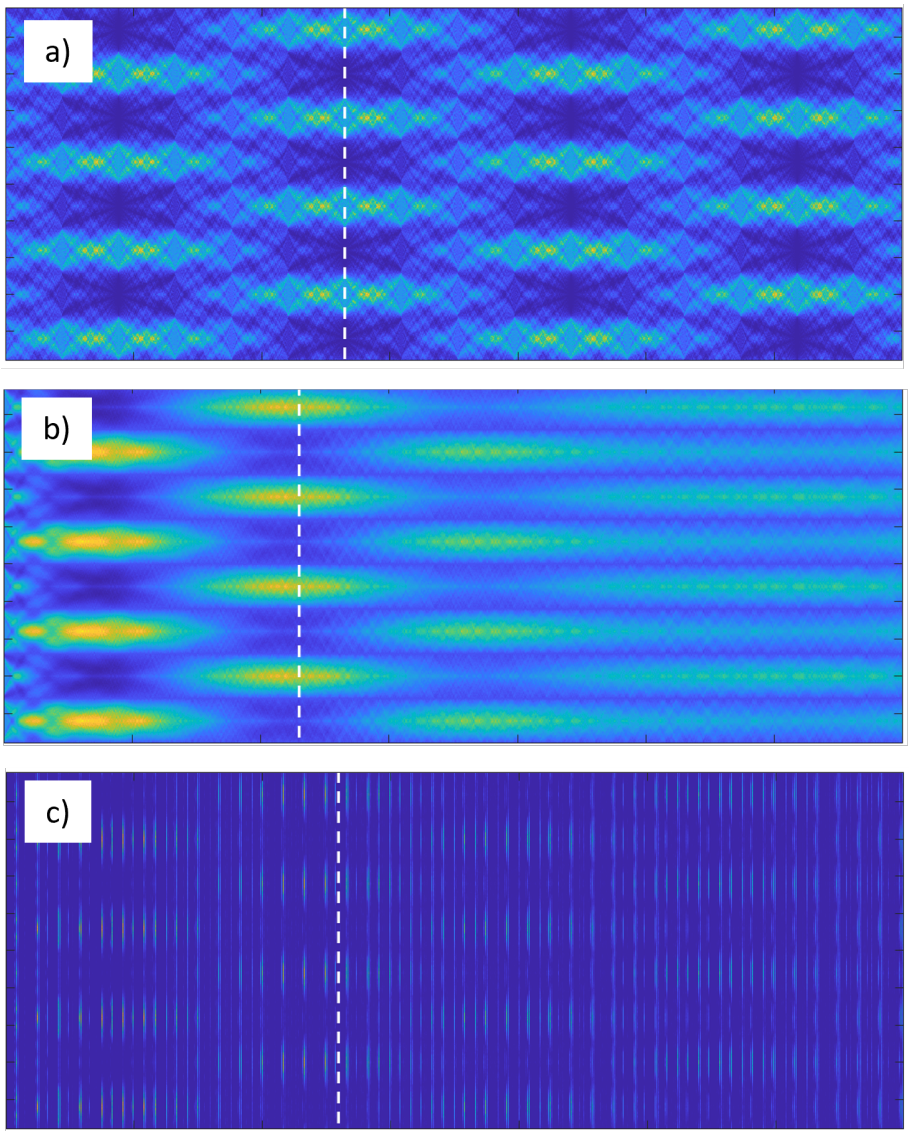

Figure 4.4: Talbot patterns of multiple beam chromacity: a) a monochromatic beam at 37.5 keV; b) a uniformly distributed photon energy spectrum; and c) a photon energy configuration conducted from Figure 4.3. The white dashed line in each pattern indicates the third fractional Talbot distance, calculated using the effective energy.

distribution. Consequently, the question arises: what impact will this have on curve-fitting and the subsequent determination of Fourier series coefficients, which are essential for reconstructing the three image modalities?

4.2 Visibility Investigation

The visibility analysis begins with the questions posed in the previous subsection and continues with interference pattern intensity comparison and Fourier series extraction.

4.2.1 Curve Fitting Comparison

With three Talbot interference patterns obtained (Figure 4.4), the next step in the phase-stepping method pipeline is to plot and fit their intensity distributions using Fourier series. Subplot c) of Figure 4.4, generated using the imaging experiment's beam configuration, is further expanded into two patterns, presented alongside subplot a) in Figure 4.4. Subplot c) of Figure 4.5 is specifically determined by selecting photon energy bins to align the effective energy with the phase grating's design energy, outlined in Tab. 4.1 (Measurement II), leveraging the energy-resolved capabilities of the TimePix 3 detector. The Bin of Interest (BoI) applied for generating this subplot is further utilized for image optimization, as detailed in the next chapter.

Thus far, we have mathematically modeled the interference patterns achieved in our imaging experiments, although their direct measurement is limited by the detector's spatial resolution. The

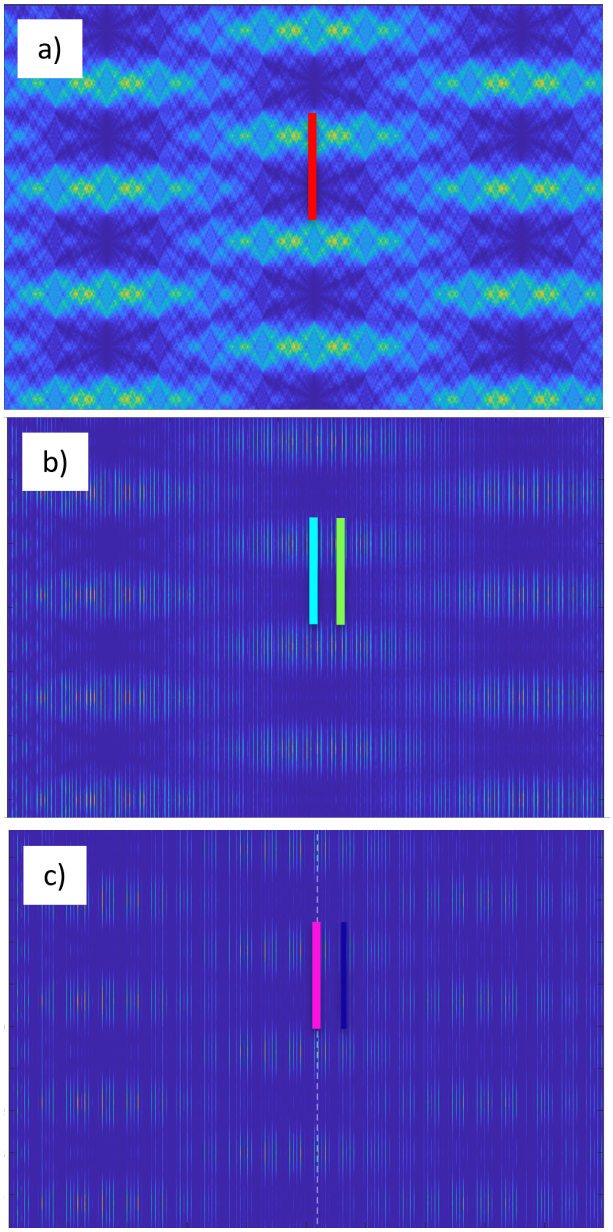

Figure 4.5: Talbot interference patterns (expanded from subplot c of Figure 4.4) under different incident photon energy distribution conditions: a) monochromatic 37.5 keV beam (standard Talbot pattern); b) pink range beam configuration from Figure 4.3 (simulated, effective energy: 33.7784 keV); c) energy bin of interest (BoI: 35-43 keV) from Tab. 4.1 (simulated to match design energy's effective energy). Colorful lines mark selected positions for plotting intensity distributions over one pattern period, with consistent colors maintained for corresponding plots and curve-fitting in Figure 4.6

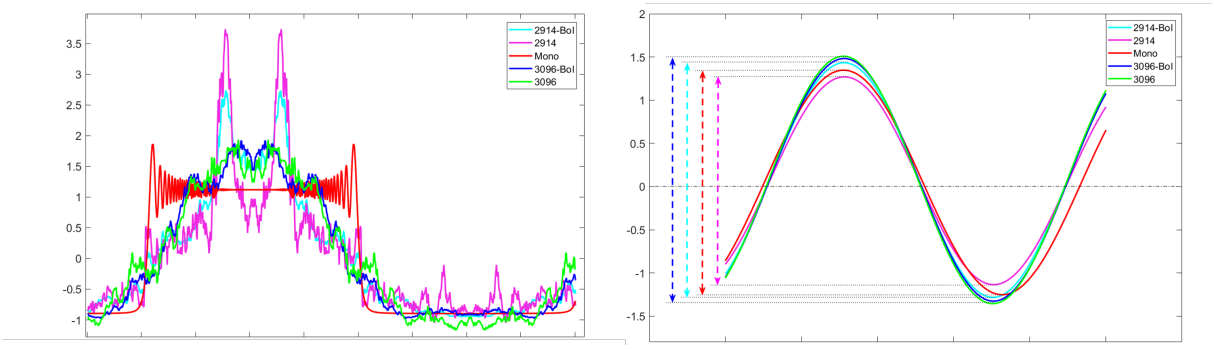

Figure 4.6: Lateral intensity profiles (left) and corresponding fitted curves (right) at various downstream positions. Each numerical label indicates a specific measurement location along the beam path, as seen in Figure 4.5.

lateral intensity distribution varies along the beam propagation, as evident in the interference patterns. We investigated the intensity profile at the third fractional Talbot distance (frTD) for all three patterns, marked as red, light blue, and pink lines in each subplot of Figure 4.5. We also studied the intensity profiles at the experimental detector distance after the phase grating in the imaging measurement, indicated by the green line in subplot b) and the dark blue line in c). Figure 4.6 presents fitted curves of selected intensity profiles, maintaining consistent color labels from Figure 4.5. Subsequently, the coefficients of each fitted sine curve are processed to calculate visibility, a procedure detailed in the following subsection.

4.2.2 Visibility Analysis

This visibility analysis explores the numerical differences in Fourier series coefficients and the resulting dark-field imaging signal visibility (calculated via Eq. 2.7) among the interference patterns shown in Figure 4.5. Table 4.2 presents the ratios of visibility values calculated from the curves on the right side of Figure 4.6. The

numerical positions indicate: 2914 - the third fractional Talbot distance for the monochromatic 37.5 keV Talbot pattern (f_3); 3096 - the detector position during the screw imaging experiment (f_3 + 16.5 mm); and 2850 - the third frTD determined by the effective energy of 33.8295 keV for the polychromatic Talbot pattern (subplot c) of Figure 4.4). These values suggest a correlation between data processing and detector positioning. Specifically, sorting the original measurement data into two groupsfull photon energy spectrum and a bin of interest aligning to 37.5 keVreveals that better visibility can be achieved either by applying the full spectrum data to image computation with the detector positioned at the frTD calculated by effective energy of the full spectrum, or by selecting specific photon energy bins for processing with the detector positioned as accurately as possible at the frTD of mono-energy 37.5 keV. Based on this, the dark-field image of the measured metallic screw is predicted to have better quality when using the full photon energy spectrum compared to the image generated from BoI data, as indicated by the visibility ratio of 0.9649 in Tab. 4.2.

Table 4.2: Comparison of Visibility Across Modeled Interference Patterns.

Position	2914 (f_3)	3096 (f_3 + 16.5 mm)	2850 (255.4 mm)
Ratio (BoI/Full)	1.005	0.9649	0.9007

The visibility values presented in Tab. 4.2 were derived from the mathematical model of the interference pattern, using the beam configuration from the imaging measurement. Additionally, a set of visibility values calculated from the reference measurement data was investigated and is shown in Tab. 4.3. Specifically, for the reference

measurement, the visibility values in each pixel of the TimePix3 detector were processed using a normal distribution to calculate the average ratio and expectation value. Since the reference measurement involved no object to induce distortion, the visibility across all pixels should theoretically be uniform. Consequently, the 2D visibility map of all detector pixels, as seen in Figure 4.7, shows an even distribution, although some imperfect pixels with outlier values are observable. These bad pixels, potentially caused by poor fitting or intrinsic defects in the detector pixel matrix, can introduce noise into the reconstructed dark-field image.

Table 4.3: Comparison of Visibility Between Model and Experimental Data, Value (Min, Max)).

Data resource	3096 of Pattern	Average Value	Expectation Value
Ratio (BoI/Full)	0.9649	0.8785 (0.8199, 0.9343)	0.8749 (0.8694, 0.8877)

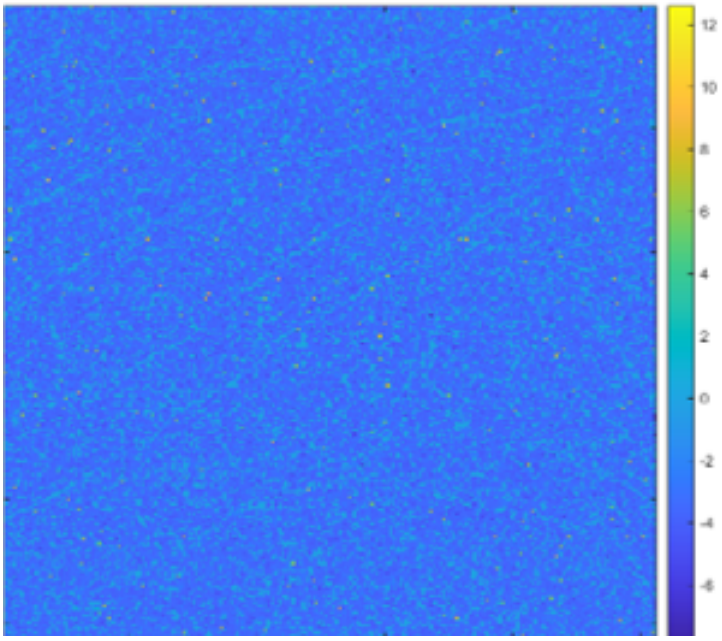

Figure 4.7: Visibility map of the grating interferometer, determined by the proposed setup and methods (All Bins), averages -4.6634 ś 0.1654.

4.3 Additional investigation

4.3.1 Photon Energy Spectrum of Imaging Experiment

To further investigate the influence of the X-ray tube's photon energy distribution on the final image results, spectra were measured under various conditions and are shown in Figures 4.8, 4.9, and 4.10. Comparing Figure 4.8, which displays the original photon counts, to Figure 4.9, which shows the normalized photon counts per energy bin, reveals that the object in the beam path caused minimal spectrum shifting, primarily resulting in a peak reduction due to photon absorption by the metallic screw.

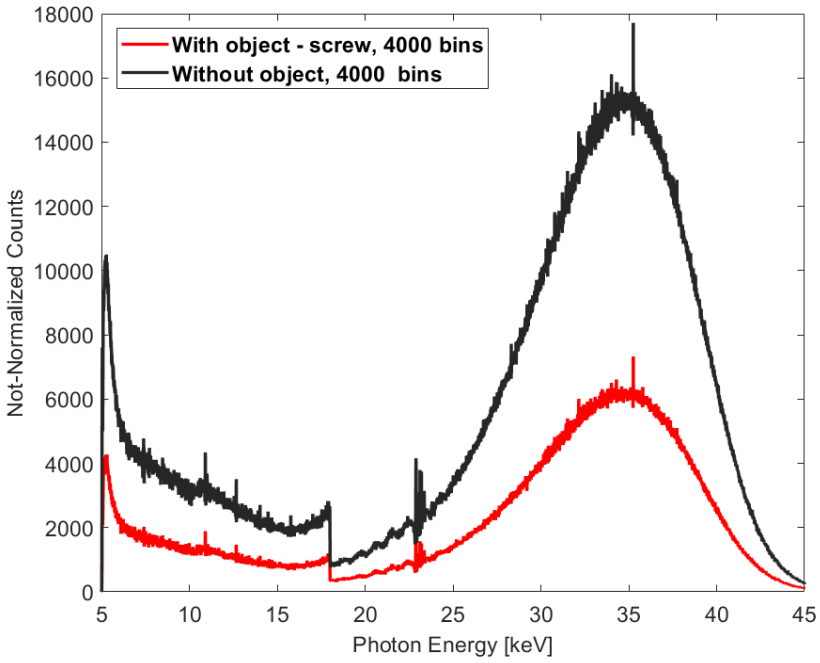

Figure 4.8: spectrum of screw imaging measurement reference and with the object within the beam path

A slight shift in the count peak is evident in Figure 4.10 when the grating interferometer is introduced into the beam path. To achieve the desired effective energy through the BoI selection, the

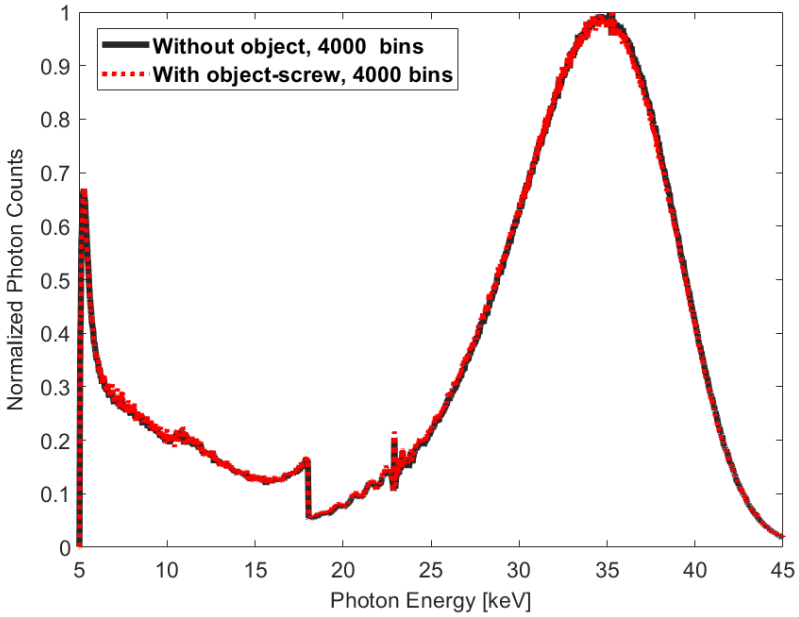

Figure 4.9: Normalized spectrum of screw imaging measurement reference and with the object within the beam path

total counts within the BoI were ensured to be 75% of the full spectrum. However, a dramatic reduction in photon flux occurred after grating insertion, indicating a significant challenge in adding a third grating (source grating) due to the risk of insufficient counts and subsequent noise.

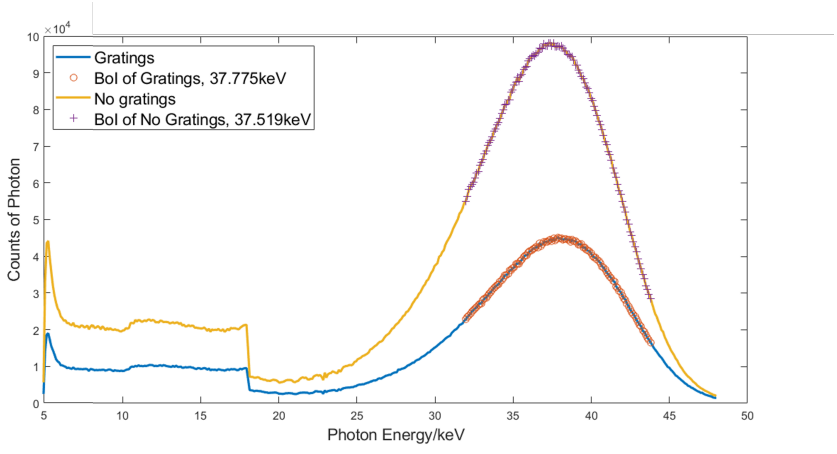

Figure 4.10: Spectrum testing with and without gratings- Experimental parameters are presented in Measurement II of Section 4.1.1

4.3.2 Fresnel Diffraction Simulation

To further investigate the intensity distribution of the interference pattern at the fractional Talbot distance (frTD), a Fresnel near-field diffraction simulation was performed using GATE (GEANT4 Application for Tomographic Emission). GATE is a Monte Carlo-based simulation toolkit known for its well-validated physics modules and robust geometry description for simulating photon-matter interactions [60–62]. In this PhD thesis, the Fresnel diffraction simulation code, adapted from Langer et al.'s work on modeling Fresnel diffraction for X-ray phase contrast imaging simulations [63], was aligned with the geometry of Measurement II (Section 4.1.1). Replicating the experimental phase grating G1, the simulated object's geometry was configured with specific parameters: 200 μm silicon substrate, 3.6 μm high lithographed gold bars (inducing a $\pi/2$ phase shift at 37.5 $\pm$ 0.5 keV), 2.4 μm period, and a 0.5 duty cycle. To align with experimental conditions where the detector's pixel size was approximately 12 times the calculated interference pattern period, the simulated object was configured. This object, which contained 12 grating periods, was set to occupy a volume of 48 μm (x) Œ 5 μm (y) Œ 203.6 μm (z) in the beam path. In the simulated imaging configuration, the grating bars were aligned with the y-axis, the x-axis represented the transverse direction perpendicular to the bars, and the z-axis was set as the propagation direction. In this simulation, illumination was provided by a polychromatic plane wave with effective energy at 37.5 keV. As predicted by Eq. 2.2, the interference

pattern exhibited a period of $p_t = p_1 = 2.4$ μm. To facilitate the accurate detection of these patterns, the virtual detector's resolution was deliberately set to a very fine 0.0078 μm. This resolution, being approximately 300 times smaller than the pattern period, allowed for the precise capture of intensity variations. Given the grating's uniform structure along the y-axis, the simulated Fresnel pattern is effectively one-dimensional and is consequently depicted as an intensity distribution, which can be observed in subplot a) of Figure 4.11. The intensity profile reveals distinct features. Within its two highest peaks, twelve lower-amplitude sub-peaks are visible at equal intervals, correlating precisely with the twelve grating periods set in the object's geometry. The subplot of b) in Figure 4.11 provides a zoomed view of the central profile range, indicated by the red double arrow in subplot a), highlighting that the central eight of these sub-peaks show greater regularity in amplitude and period than those at the profile's extremities. Furthermore, beyond these maximum peaks, denser, very low-amplitude fluctuations are observed, attributable to edge diffraction from the object's physical boundaries.

To simulate the sampling procedure inherent in a phase-stepping methodwhere an analyzer grating samples the intensity profile's fluctuations with specific phase incrementswe performed a manual segmentation of the simulated Fresnel pattern. Specifically, the intensity data from eight selected periods were individually extracted and separated. This process involved rescaling and accumulating these eight separate patterns to construct a single, representative

period profile, as depicted in as depicted in the subplot c) of Figure 4.11. In this conceptualization, the intensity from the central eight peaks of the profile (shown in subplot b)) would typically be captured by individual detector pixels in a real experiment. By comparing these rescaled profiles with the intensity profiles from the mathematical model (left side of Figure 4.6), it reveals a similar profile distribution, which is the imperfect rectangular shape with ignorable subtle fluctuations at the top compared to the amplitude. Given that the mathematical method for deriving the visibility value of this rescaled profile mirrors the approach presented in Subsection 4.2.2, we omit the detailed repetition of the fitting and coefficient generation. Consequently, this Fresnel diffraction simulation study predicts a promising visibility value, as demonstrated in Subsection 4.2.2.

Following the approach in Subsection 4.1.3, a photon energy spectrum study was performed using the Fresnel diffraction simulation, employing a one-period phase grating object. The patterns and intensity profiles obtained are presented in Figure 4.12. This study of investigation demonstrated that the intensity profiles exhibited remarkable stability across varying photon energy configurations. Notably, the one-period pattern extracted from the bin of interest (BoI) spectrum was in close agreement with the monochromatic beam simulation. This finding demonstrates the applicability of the principle of superposition for wave fields incorporating multiple wavelengths, thereby confirming the consistent behavior of the overall wave field regardless of its spectral composition. It further

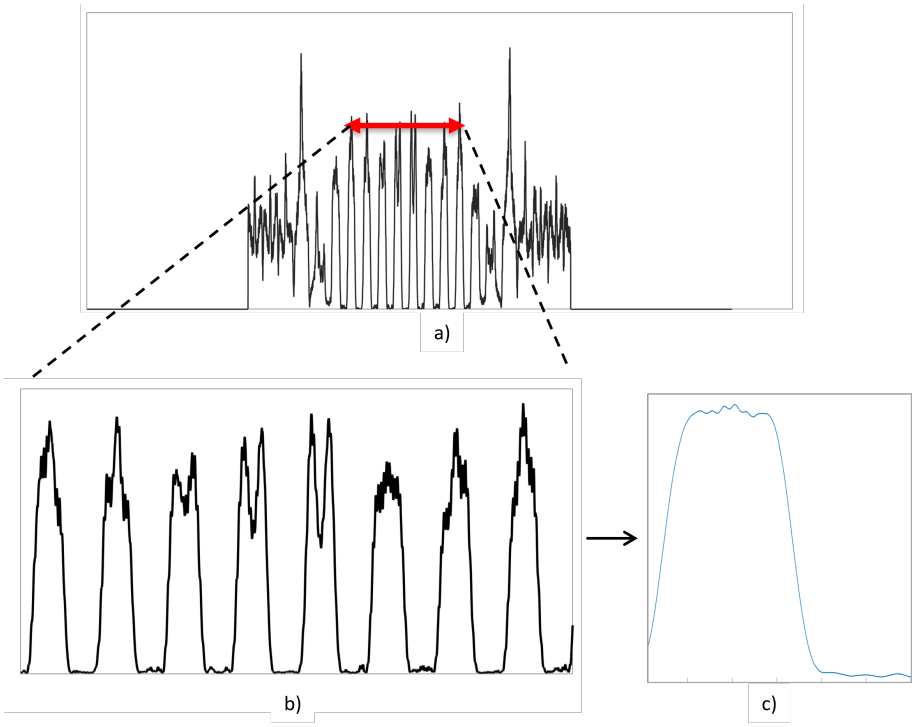

Figure 4.11: fresnel diffraction simulation with outlined beam configuration in Figuer 4.3: a) intensity of the simulated pattern; b) selection of a range of intensity plot in a); c) rescaled intensity profile into one period. By comparing the rescaled profiles with the intensity profiles from the mathematical model (left side of Figure 4.6),it reveals a similar profile shape, predicting a promising visibility value, as investigated in Subsection 4.2.2

indicates that a promising approach for simplified, compact X-ray interferometry dark-field imaging involves combining a conventional microfocus X-ray tubewhich yields a polychromatic beam with partial spatial coherencewith a pixelated, energy-resolving photon-counting detector. This detector enables photon energy selection during data processing to optimize spectral coherence and thus enhance the interferometric effect.

4.4 Summary of Chapter 4

The primary focus of this PhD work is the development of an X-ray interferometry-based dark-field imaging setup that utilizes a partially spatially coherent X-ray source. Since the interferometric

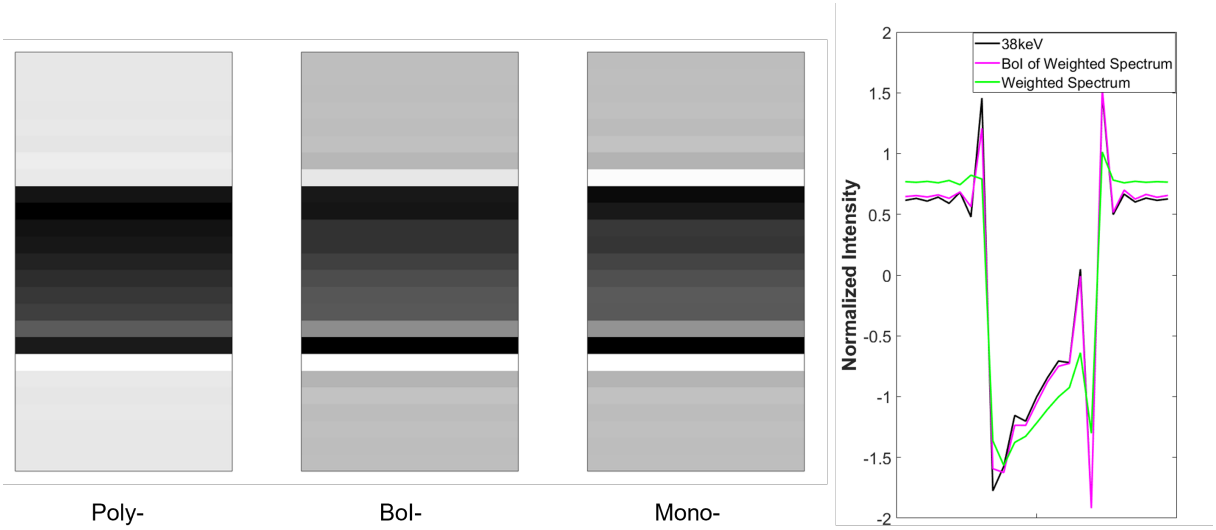

Figure 4.12: Photon energy spectrum study in Fresnel diffraction simulation – observation of one period pattern with various incident beam configurations. The intensity profiles exhibited remarkable stability across varying photon energy configurations. Notably, the one-period pattern extracted from the bin of interest (BoI) spectrum was in close agreement with the monochromatic beam simulation.

effect is highly dependent on the incident beam's coherence, a significant challenge in this endeavor involves characterizing the beam's properties and their impact. Consequently, this chapter employs mathematical modeling (applied in the MATLAB platform) and Fresnel diffraction simulation (using the GATE toolkit) to comprehensively investigate how beam parameters affect the interference pattern's visibility.

The results indicate that similar interferometric effects can be evaluated across various beam conditions, suggesting a promising feasibility for dark-field imaging with the proposed setup. However, potential noise issues, which will be addressed in the subsequent chapter, were also identified.

Furthermore, the selection of experimental data according to photon energy bins (BoI of X-ray spectra) may have a minor impact on visibility contrast, resulting in either an improvement or a

degradation, depending on the detection location. Additionally, the study suggests that relatively high-quality phase contrast imaging can be achieved using the same compact setup by selecting data from specific photon energy bins. This capability is facilitated by energy-resolved imaging photon counting detectors like, e.g., the Medipix family.

5

Image Reconstruction, Discussion and Optimization

Based on the investigation of the proposed setup in the previous chapter, this chapter explores image optimization methods designed explicitly for this X-ray interferometry setup.

This chapter employs several key terms and processing methods that need to be specified:

Pattern Period (p_t): This refers to the period of the lateral intensity profile observed at the detector position in Measurement II. Specifically, this position is located at the third fractional Talbot distance (f_3) plus 16.5 mm, as specified in Tab. 4.2, referencing '3096'.

f_3: This denotes the third fractional Talbot distance for 37.5 keV X-rays, calculated using a 2.4 μm period, $\pi/2$ phase grating.

All-Bins: This represents the complete set of original experimental data in each detector pixel from Measurement II, sorted by digital photon energy bins, and processed using the phase-stepping methods for image reconstruction.

Bin of Interest (BoI): As a comparative analysis to All-Bins, this refers to a selected range of data, determined by specific photon energy bins to ensure a 37.5 keV effective energy, and used for image

reconstruction. The selection range is specified in Table 4.1.

5.1 Fitting Equations for Image Reconstruction

5.1.1 Two Fitting Equations: Eq-I and Eq-II

As observed in the initial image results of the screw (Figures 3.4 and 3.5), the attenuation and dark-field images in the latter figure of the screw, compared to former, showed an improvement of visual representation of the pitch structure. The thread edges of the screw in both dark-field images are more distinct and more straightforward to discern than in any of the attenuation images. Consequently, the pattern period (p_t), though theoretically a constant, was included as a variable in the fitting equation (Eq. 3.1). This was done to improve the fit's reliability by allowing the iterative algorithm to account for potential small deviations in the pattern period (p_t), which, while theoretically constant, might exhibit minor variations in experimental data. This extended equation, denoted as Eq-I throughout this PhD thesis, was preferred over Eq. 2.5 for the image optimization process.

Moreover, mathematically, Eq-I can be transformed to the following form:

$$I(x_g)^i = a_0^i + \sum_{n=1}^{\infty} \left[a_n^i \cos\left(2\pi n \frac{x_g}{p_t^i}\right) + b_n^i \sin\left(2\pi n \frac{x_g}{p_t^i}\right) \right] \qquad (5.1)$$

Here, i refers to the pixel index. x_g denotes the position of the analyzer grating along the lateral direction of the grating bars. Restricting the equation to the first harmonic terms (n=0, 1) simplifies

it to:

$$I(x_g)^i = a_0^i + \left[a_1^i \cos\left(2\pi \frac{x_g^i}{p_t^i}\right) + b_1^i \sin\left(2\pi \frac{x_g}{p_t^i}\right) \right] \tag{5.2}$$

This simplified equation, keeping only harmonic terms compared to Eq. 5.1, is referred to as Eq-II. The coefficient matrix $C^i(a_0^i, a_1^i, b_1^i, p_t^i)$ was generated by curve-fitting with given step x_g and measured data $I(x_g)^i$ of the i^{th} pixel. The image signals in each pixel were then computed by substituting the coefficients into Eq. 2.8, 2.9,and 2.10 to achieve attenuation, phase contrast, and dark-field image, respectively. The following sections will compare image reconstructions using Eq-I and Eq-II. The reason to perform this comparison is that the curve-fitting algorithm relies on iteration, and Eq-II, with its two trigonometric terms, provides an additional channel compared to Eq-I, potentially leading to a better fitting effect, as suggested by Velroyen et al. [64].

Furthermore, an investigation into the impact of photon energy distribution on image results was conducted, which involved processing the original experimental data using two distinct groups: All-Bins and Bin of Interest (BoI), whose definitions were provided at the beginning of this chapter. Both datasets were processed using the phase-stepping procedure described in Subsec. 2.2.2, without any further modifications.

5.1.2 Screw Image Results Using Eq-I and Eq-II

Within the scope of this PhD work, dark-field and attenuation images are presented collectively. Due to the significant challenges posed by weak wave coherence within the proposed setup and

method, the phase contrast images are presented and discussed individually later.

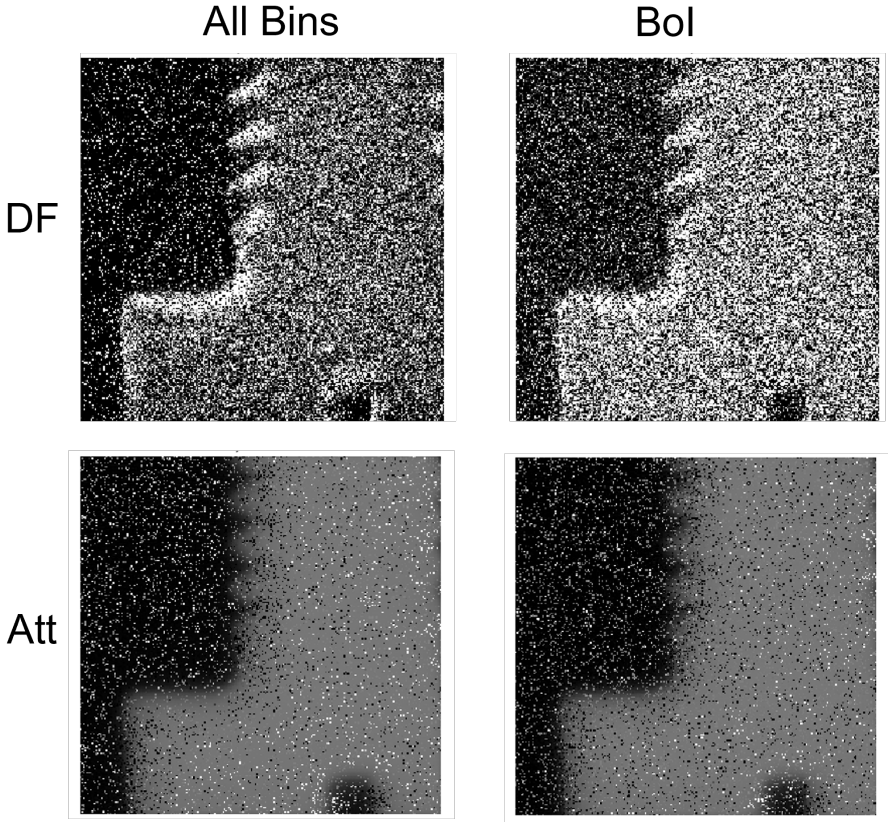

Figure 5.1: image reconstructed based on Eq-I

The comparison of All-Bins vs BoI through Eq-I is illustrated as 4 subplots, as seen in Figure 5.1. The top row shows the dark-field images reconstructed by the data set All-Bins and BoI, where the bottom row refers to the attenuation images in the two categories. The dark-field images from both columns show sharper threaded edges, compared to attenuation images. While comparing images from the left column to the right, there is no obvious improvement from All-Bins to BoI-based images. This result also matches the investigation of visibility outlined in Chapter 4.

With a focus on dark-field images, Figure 5.2 cross-compares four dark-field images. The left column displays dark-field screw

images reconstructed from 'All Bins' data using Eq-I (top) and Eq-II (bottom), while the right column shows images from 'Bin of Interest' (BoI) data. Visual inspection suggests that the BoI dark-field images exhibit more noise than the All-Bins images, a preliminary observation that requires further statistical validation. The potential cause of this noise in the BoI images is a statistical data shortage, as the BoI range represents only about 35% of the total counts (half of the pink region) in the full histogram spectrum in Figure 4.3.

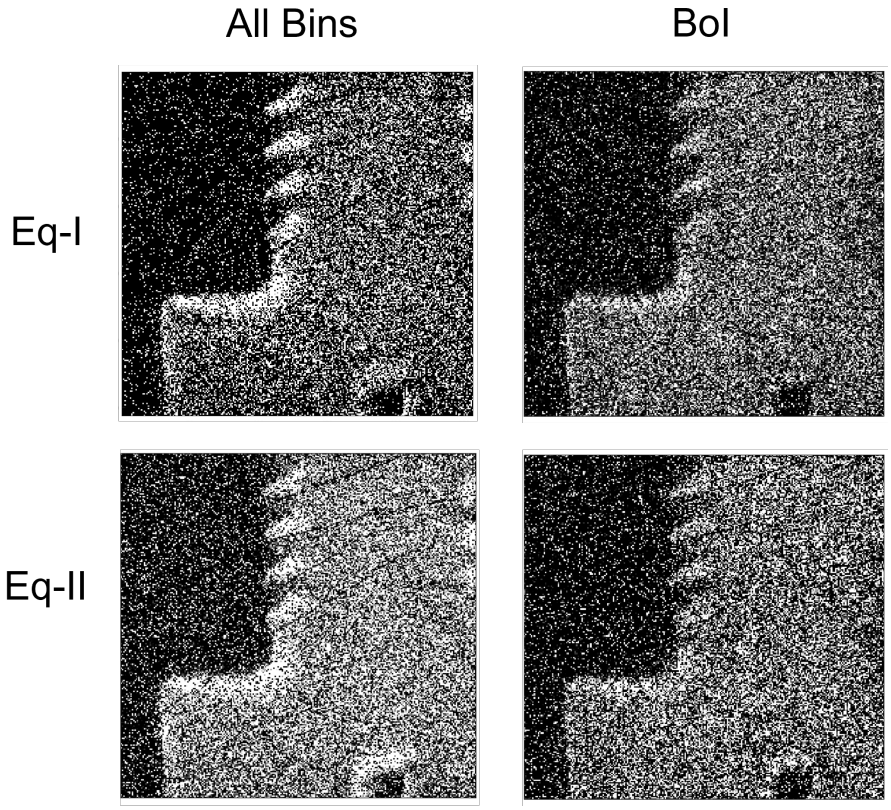

Figure 5.2: Dark-field images reconstructed based on different data selection and fitting equations

Moving from the top to bottom row, the screw thread edge appears more continuous with stronger signals from small-angle scattering due to the fine thread line structure (0.5 mm pitch).

While the background noise increases in the bottom row, Eq-II's improved fitting capability reveals detector defects as suspicious lines, which are hardly visible in the top row dark-field images.

5.1.3 Dark-field Image Analysis

For dark-field image analysis, background regions were defined as free-space photon paths, and signal regions as thread line edges due to small-angle scattering from the fine structure. A set of fixed masks, applied to all four dark-field images in Figure 5.2, was used to select these regions of interest (RoIs), as shown in Figure 5.3. This figure illustrates the background (left) and signal (thread line edge, right) RoIs, both covered by their transparent blue masks.

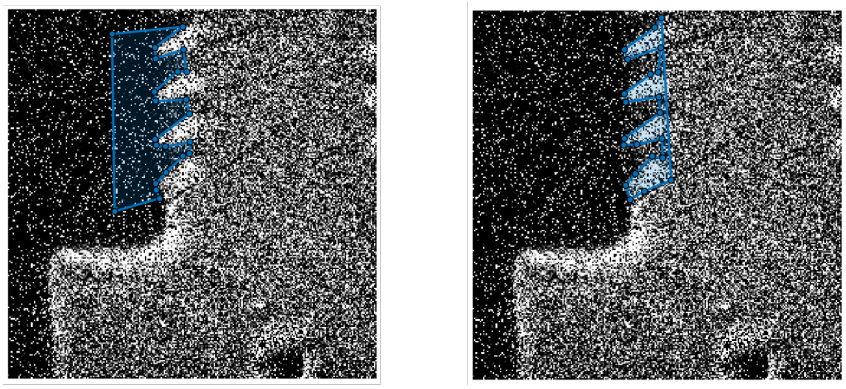

Figure 5.3: Selection of background and signal (thread line edge) regions of interest (RoIs), both covered by a transparent blue mask, individually.

The SNR and CNR were calculated using the following equations:

$$SNR = \frac{\text{Value of Signal RoI}}{\text{Standard-deviation of Background RoI}} \tag{5.3}$$

and,

$$CNR = \frac{\text{Value of Signal RoI} - \text{Value of Background RoI}}{\text{Standard-deviation of Background RoI}} \tag{5.4}$$

In Eq. 5.3 and 5.4, the average pixel values and standard deviations for the Signal and Background Regions of Interest (RoIs) were calculated directly from the pixel values within each RoI. To mitigate the potential impact of noisy pixels in both regions, a Gaussian distribution was fitted to the data of each RoI to estimate the statistical expectation (mean) and standard deviation. These Gaussian-derived parameters were then used to calculate fitting-based CNR and SNR, aiming to enhance statistical robustness.

Figure 5.4 illustrates these two dark-field image analysis methods. The top section (a) initially displays the integrated pixel value histograms for the signal and background RoIs, from which CNR and SNR were calculated using the histogram averages. Subsequently, the bottom section (b) presents the Gaussian distributions fitted to these data, and the final CNR and SNR values were derived from their fitted expectation and standard deviations.

The quantified quality assessment of the four dark-field images in Figure 5.2, based on CNR, is presented in Figure 5.5. This assessment was performed using the identical RoI selection mask (Figure 5.3) and calculation process (Figure 5.4) for all images. Within Figure 5.5, the left bar sets, labeled CNR-Histogram, correspond to the calculation method described in Figure 5.4 a), while the right bar sets, labeled CNR-Fitting, represent the results obtained using the Gaussian fitted method from Figure 5.4 b).

A significant difference exists between CNR calculated from histogram averages and those derived from fitted Gaussian expectations. This disparity is primarily due to an outlier peak near

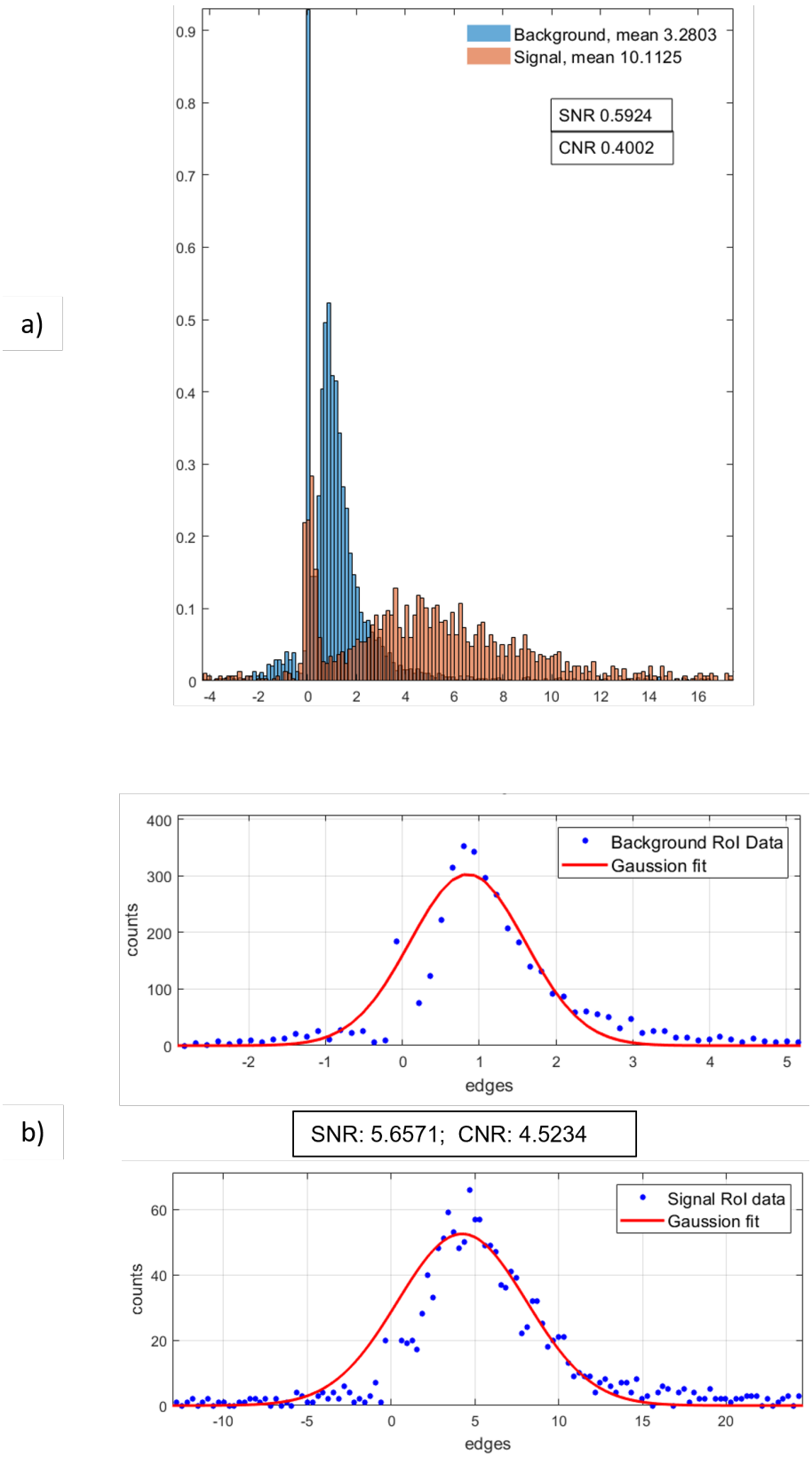

Figure 5.4: Calculation process for dark-field image analysis. a), Integrated signal and background RoI probability histograms, with CNR and SNR values calculated from histogram averages. b), Distributions of background and signal RoI data, fitted with Gaussian curves, showing CNR and SNR values based on Gaussian expectation.

zero in both background and signal RoIs, which pulls the average values away from the main peaks (background near 1, signal near 5). These near-zero values, which appear as noisy pixels in the dark-field images, will be addressed in the image optimization section.

A comparison of the results for evaluating the two equations reveals that the CNR obtained from Eq-II (represented by red bars, labeled $Eq2$ in the plot) is generally superior to that from Eq-I (blue bars, labeled $Eq1$). This trend holds true across all cases, with the notable exception of the AllBins-CNR-Fitting scenario.

Comparing CNRs between the images using All Bins and those using BoI of spectrum, a decrease in CNR for dark-field images reconstructed based on data selection of BoI is seen in the initial three bar sets. However, the rightmost bar set (Eq2-BoI-CNR-Fitting) shows an opposite trend, suggesting strong Gaussian-distributed noise in the reconstructed dark-field images based on the fitting Eq-II applied for selected data of BoI, allowing for effective denoising to potentialy acquire a higher CNR. Conversely, dark-field images based on the fitting Eq-I show a trend of decreasing CNR from the database of All Bins to BoI, possibly due to the absence of a beneficial fitting channel, preventing effective Gaussian denoising. For CNR-Histogram, regardless the dark field images reconstructed based on fitting Eq-I or Eq-II, both evaluated CNR values show a similar decrease from the dark field images calculated by utilizing the data of All Bins to those acquired by the date of BoI, likely due to the significant drops of photon count (35% of All Bins), degrading

the statistical probability of background and signal distributions, which is challenging to compensate by fitting modification (Fitting equations preference) or coherence optimization (BoI selection to align with system design energy).

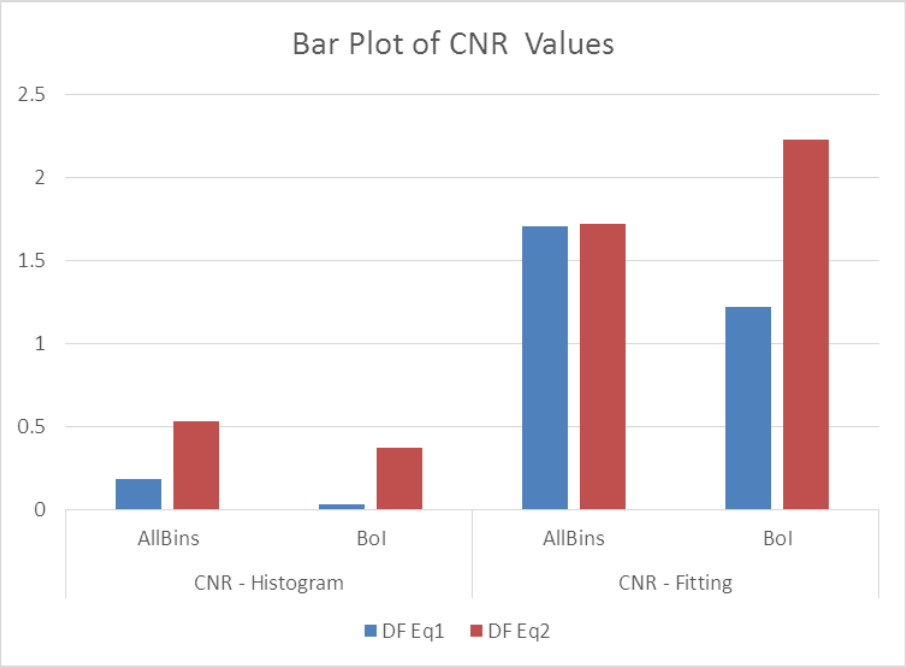

Figure 5.5: Dark-field image analysis. CNR of DF images reconstructed based on Eq-I and Eq-II. Eq-I in plot is noted as Eq1, while Eq-II as Eq2.

5.2 Optimization one: Goodness of Fitting Selection

From this point forward, the optimization will focus solely on images reconstructed using Eq-II due to its superior CNR evaluation compared to Eq-I.

5.2.1 Method of Optimization

As discussed in previous chapters, the curve-fitting step for some pixels deviated from the theoretical model, leading to imperfect fits. Consequently, these poorly fitted pixels, characterized by a low goodness of fit, were suspected to degrade the screw image

quality. To mitigate this, a filtering condition was implemented during Fourier series coefficient generation, see documents of applied code in the third and forth section of the Appendix A.2, where pixels with a goodness of fit below a certain threshold (e.g., 0.5) were treated as empty pixel values with assigned 'NaN' values in the data array of MATLAB.

While the filtering of poorly fitted pixels aimed to improve image quality, it resulted in numerous pixels having empty pixel values while generating the Fourier series coefficient for image reconstruction, paradoxically increasing the noise compared to that of the unfiltered images. To address this, these empty pixels were filled using interpolation, with the MATLAB code sourced from an open repository [65]. The interpolation script offers five methods for repainting empty pixels. For this optimization process, methods 1 and 2 were applied due to their distinct impact, a difference not observed with the other methods. Both methods utilize the Laplacian operator ∇^2 in a 2D discrete grid. The Laplacian essentially measures the difference between a point's value and the average of its neighbors. Specifically, method 1 is a global operation followed by a local selection around the missing data, with an implicit least squares fitting involved in determining the fill values, while method 2 is a local method that directly enforces a smoothness constraint (Laplacian close to zero) at the missing data points by solving a linear system.

To operate the optimization, four different levels of fitting threshold, besides zero, were set during the Fourier series coefficient

generation, which were 0.15, 0.5, 0.75, and 0.85, followed by an interpolation to refill those empty pixels while increasing the threshold of goodness of fitting.

5.2.2 Optimized Dark-field Images

Figure 5.6 shows the filtered dark-field images in the left column and the corresponding interpolated results in the right column. Interpolation method 1 was fully employed for optimizing the five reconstructed images based on various fitting thresholds. The entire plot can be visually divided into two distinct groups. Group 1, comprising the four images in the bottom two rows, clearly exhibits suboptimal optimization, characterized by blurred thread edges and anomalous bright pixel clusters. Group 2, including the six images in the upper three rows, shows a slight increase in noise level from top to bottom. This trend signifies an increasing threshold for the goodness of fit. When focusing on the impact of interpolation optimization, it's evident that the noise level in the images on the right-hand side is significantly decreased compared to their counterparts on the left-hand side. Upon reviewing the optimization effects on both attenuation (Figure 5.8) and phase contrast images (Figure 5.9), a threshold of 0.5 emerges as a strong candidate. This value appears to effectively balance the optimization across all three image types within a single procedure, thereby suggesting a potential standard method for optimizing X-ray interferometry-based imaging. Given the promising nature of this threshold, interpolation method 2 was subsequently applied to the reconstructed dark-field images

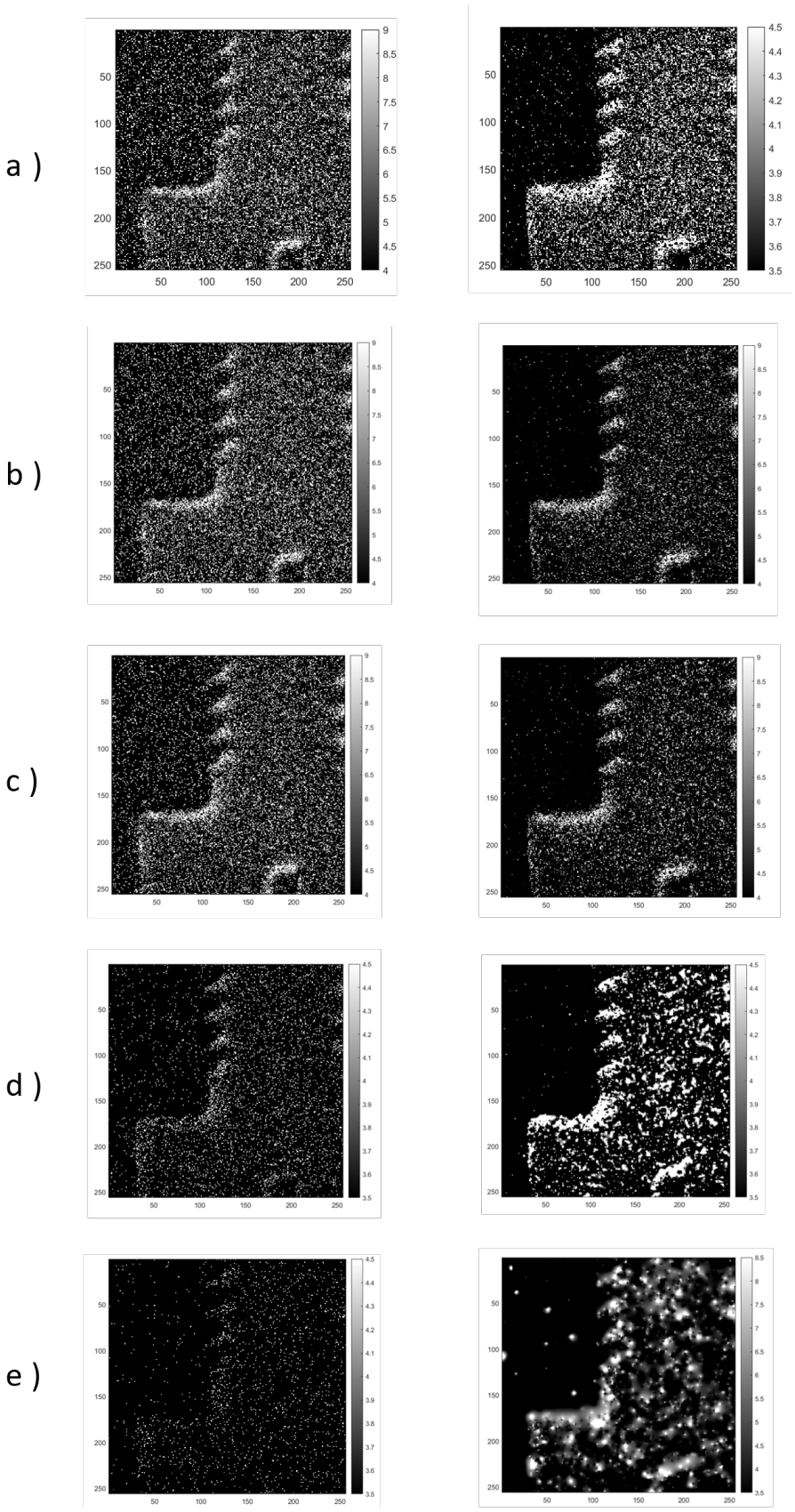

Figure 5.6: Reconstructed dark-field images of different GoF (goodness of fit). Each row: a) 0; b) 0,15; c) 0,5; d) 0,75; e) 0,85; left column: reconstruction without interpolation; right column: Interpolated dark-field images with method 1.

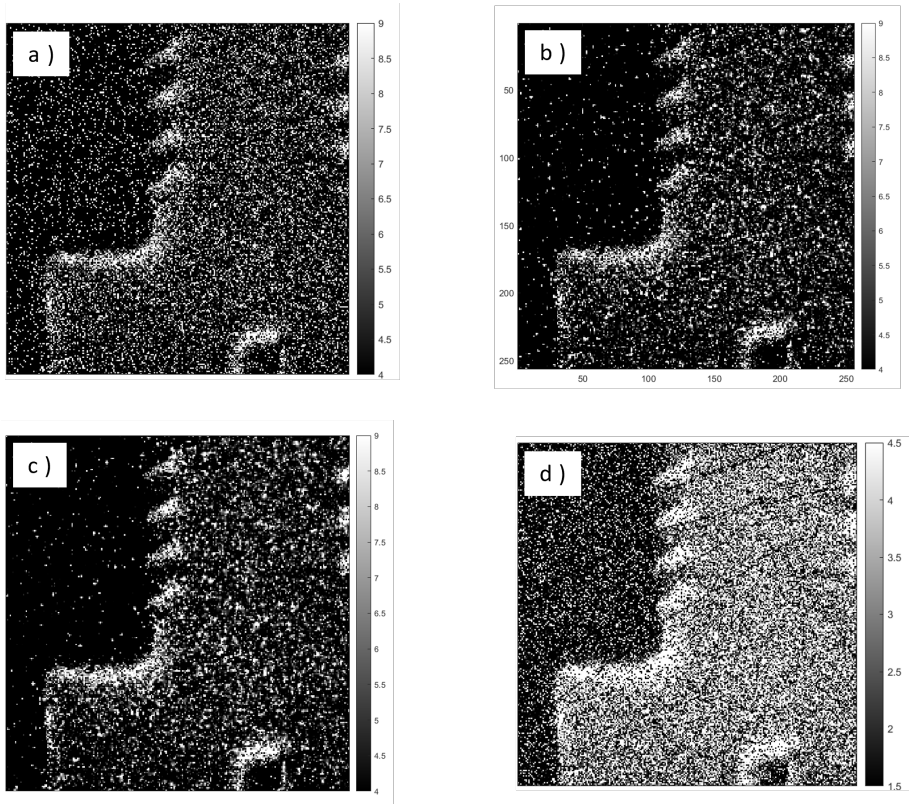

Figure 5.7: Comparison of optimized (a-c) and non-optimized (d) dark-field images, all reconstructed using Fourier series coefficients (Eq-II). Optimized images (a-c) underwent goodness-of-fit filtering (GoF ≥ 0.5) and different interpolation: a) None, b) Interpolation method 1, Global Laplacian filling (implicit least squares, global operation followed by local selection), c) Interpolation method 2, Direct Laplacian solving (local linear system enforcement). Image (d) is the direct reconstruction from the coefficients acquired through fitting Eq-II, without filtering or interpolation.

at a goodness of fit of 0.5 to further explore optimization strategies.

Consequently, methods 1 and 2 of the five available interpolation methods were selected and applied to the dark-field images filtered with a goodness of fit threshold of 0.5. These methods differ fundamentally: Method 1 performs a global operation followed by a local selection with implicit least squares fitting for filling NaN values, while Method 2 is a local method that directly enforces a smoothness constraint by solving a linear system at the NaN locations. Figure 5.7 shows the four plots of optimized dark-field images. Image d), which received no post-processing such as goodness-of-fit

selection or interpolation, exhibits a strong thread edge signal due to sufficient photon counts. However, it also retains a high noise level because noisy pixels are fully preserved. In contrast, Image a) is notably noisier than both images b) and c), primarily due to a high ratio of empty pixels that degrade its quality.

A distinct optimization effect is observed from interpolation method 1 to method 2. This suggests that refilling empty pixels by sampling from a local region significantly enhances the interpolation's effectiveness.

To quantify these optimization effects, the image evaluation based on CNR and SNR values is presented in Tab. 5.1. Both CNR and SNR were calculated based on the Gaussian expectation value, as previously introduced in Subsection 5.1.3.

Table 5.1: Comparison of the optimized Dark-field Images.

DF Images in Optimized DF Images	a)	b)	c)	d)
CNR	1.5512	1.0903	**5.2421**	1.7228
SNR	2.4746	2.4745	**7.5547**	2.5337

5.2.3 Optimized Attenuation Images

Employing the same data processing methods and goodness-of-fit filtering parameters as for the optimization of dark-field images (Figure 5.6), outlined in 5.2.1, attenuation and phase contrast image groups were acquired simultaneously, as shown in Figure 5.8 and Figure 5.9 respectively.

In the attenuation contrast images (Figure 5.8), the thread pitch of the metallic screw was heavily blurred across all subplots. Conversely, the non-threaded regions exhibited strong signals due to X-ray absorption. With increasing goodness of fit threshold, the noise levels rose in both image columns, a consequence of the greater number of empty pixels in the reconstructed images, leaving fewer reliable pixels for the interpolation to use for refilling.

Furthermore, the interpolation method effectively darkened the background only for images reconstructed with a threshold of 0.5 or lower. However, beyond this threshold, the reconstructed attenuation images (left column, rows d and e) had already lost accurate structural information, rendering the background and screw area indistinguishable. Although the corresponding interpolated images (right column, rows d and e) showed increased contrast, their overall quality remained significantly lower than the upper three rows (a, b, and c).

5.2.4 Optimized Phase Contrast Images

In contrast to the optimized attenuation contrast images, the optimized phase contrast set, as seen in Figure 5.9, yielded very few acceptable subplots, especially considering the expected strong boundary visualization inherent to phase contrast imaging.

However, combining an interpolation method with a goodness-of-fit threshold of 0.5 produced a noticeably improved image with significantly enhanced contrast at the air-object interface. Compared to the effect of optimization on dark-field imaging through the proposed setup, this observation emphasized the critical requirement of beam coherence for X-ray interferometry-based phase contrast imaging, as outlined in previous chapters. Furthermore, it highlights the importance of magnifying the interference pattern's intensity to accurately capture wave distortion, which is essential for generating high-quality phase contrast image signals.

The dramatic decrease in image contrast at higher goodness of fit thresholds could be attributed to the combined effects of weak phase shift generation due to limited beam coherence and the further degradation caused by empty pixels. Nevertheless, these limitations might be mitigated by carefully balancing the goodness of fit threshold and the subsequent interpolation of empty pixels.

For the phase contrast images corresponding to Measurement II in this PhD work, the optimal parameters appear to be a goodness of fit threshold of 0.5 during Fourier series coefficient generation, followed by interpolation method 1. It is important to note that if

experimental parameters such as X-ray tube voltage or inter-grating distance differ from Measurement II, the optimal goodness of fit threshold should be investigated individually.

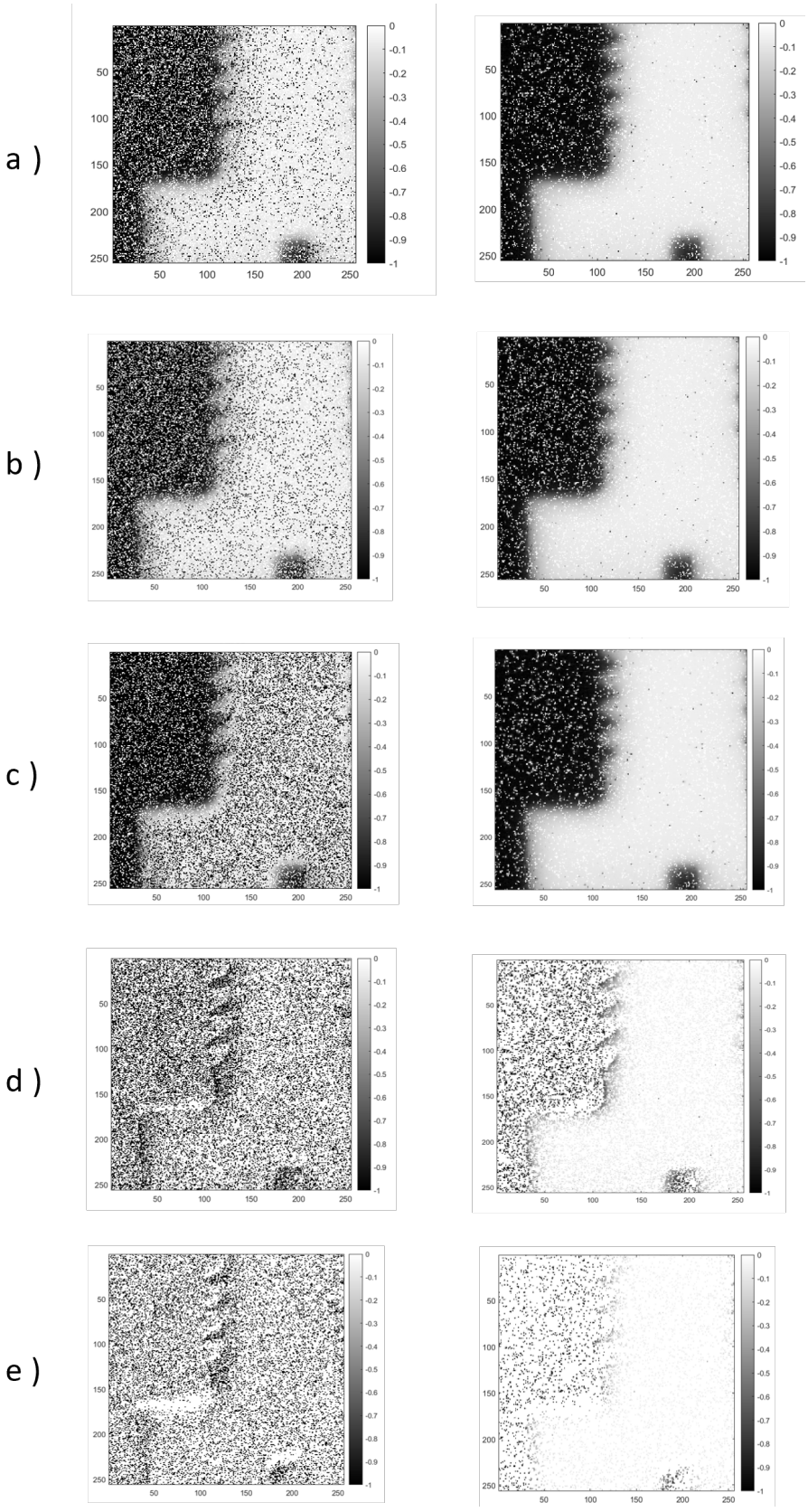

Figure 5.8: Reconstructed Attenuation images of different GoF (goodness of fit). Each row: a) 0; b) 0,15; c) 0,5; d) 0,75; e) 0,85; left column: reconstruction without interpolation; right column: Interpolated attenuation images.

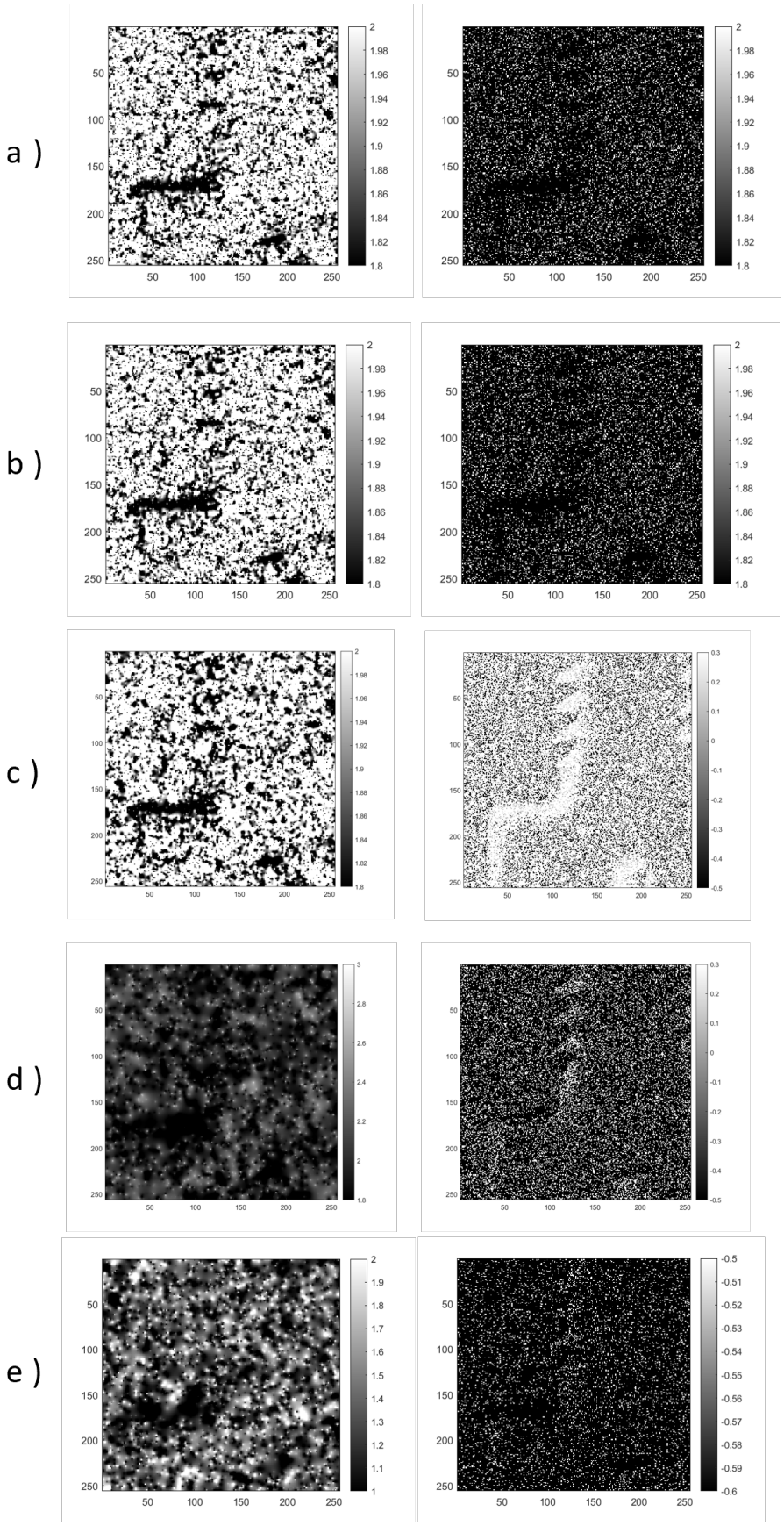

Figure 5.9: Reconstructed Phase contrast images of different GoF (goodness of Fitting). Each row: a) 0; b) 0,15; c) 0,5; d) 0,75; e) 0,85; left column: reconstruction without interpolation; right column: Interpolated Phase images.

5.3 Optimization Two: Signal Probability Distribution

As discussed in Subsection 5.1.3, the outlier peak in the background RoI histogram (Figure 5.4a) likely contributed to image noise. To achieve a uniform background visibility, a denoising optimization was implemented by manually adjusting the visibility distribution of the reference data, similar to a flat-field correction in CT imaging.

5.3.1 Probability Distribution

The objective of analyzing the pixel value probability distribution within a selected region was to establish a threshold for segregating reliable pixels from noisy ones in the signal region of interest (RoI). Initially, a small region, designated as Mark-8, was defined to target the fine structure of the screw thread pitch. This specific designation was used to maintain data processing continuity and avoid confusion with other masks. Within mark 8, three sub-regions were manually delineated: threadline bottom, threadline top, and screw neck. Figure 5.10 illustrates the determination of these regions (yellow, blue, red, and underlying gray) and the corresponding sorted probability distribution histogram of pixel values, with the y-axis rescaled to the logarithm of counts. Notably, the stacked plot of the pixel values from the three sub-regions exhibits higher counts than the entire region of Mark-8 due to the manual sub-division. While the value of a peak centered around 2.5 is observable for

the threadline bottom, the threadline top appears centered around 10, suggesting a potential signal difference between the threadline top and bottom. This could be reasonable as the screw threadline ascends, as depicted in Figure 5.11, despite the frequently depicted symmetric pitch in screw illustrations. Moreover, the probability of collecting scattered rays is likely higher from the threadline top than from the bottom. This can be explained as follows: when photons reach the threadline edge (as illustrated by the arrows), the red scattered photons directed towards the threadline top can still propagate freely to the detector. In contrast, the upper blue arrow indicates photons that are blocked and immediately absorbed after undergoing slight scattering towards the screw solid region, whereas only the lower blue arrow represents photons that can reach the detector.

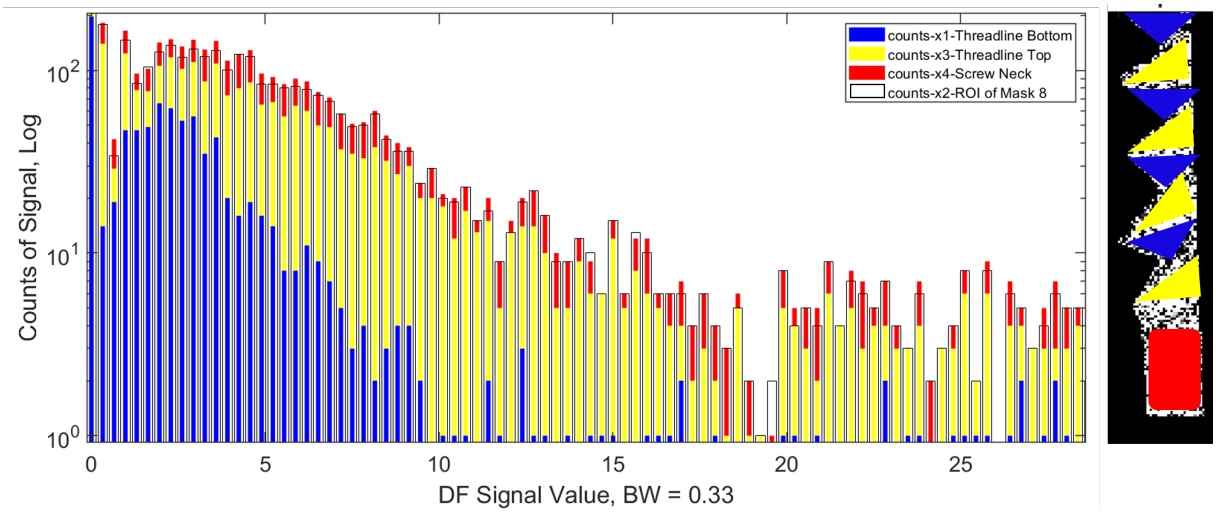

Figure 5.10: DF image pixel value distributio of signal RoI

To further define a threshold for the segregation of the signal and background, a Gaussian distribution was utilized to examine the mean and standard deviation of each sub-region. Four exper-

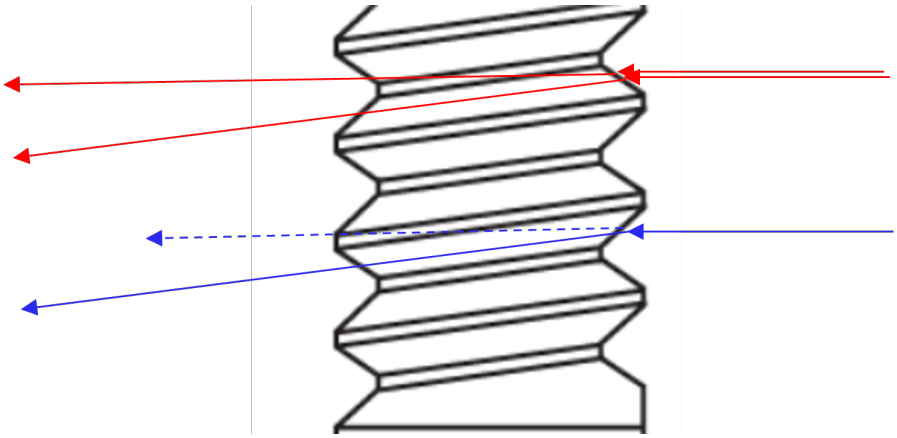

Figure 5.11: Sketch of a thread structure illustrating a non-symmetrical detail of the thread edge. When photons reach the threadline edge (as illustrated by the arrows), the red scattered photons directed towards the threadline top can still propagate freely to the detector. In contrast, the upper blue arrow indicates photons that are blocked and immediately absorbed after undergoing slight scattering towards the screw solid region, whereas only the lower blue arrow represents photons that can reach the detector

imental tests were performed, involving the manual selection of the threadline top and bottom with an attempt to maintain consistent region sizes. The upper bound of pixel values (maximum) for the threadline bottom and the lower bound (minimum) for the threadline top derived from these tests are presented in Tab 5.2. The observed overlap in the pixel value distributions of these two sub-regions, however, indicates that an alternative strategy for threshold determination is required. It is worth noting that, considering the tiny area of each sub-region, the effectiveness of the Gaussian distribution method for thresholding could be enhanced with longer measurement times or larger signal RoI that provide higher statistical confidence.

Table 5.2: Various testing for determining the threshold of pixel values.

Testing	1	2	3	4
Threaline Top Min.	3.2191	3.3328	3.0640	3.2760
Threadline Bottom Max.	3.3160	3.7089	3.6056	3.448

5.3.2 Threshold of Noisy Pixel Value

As detailed in the visibility investigation in Chapter 4, the reference data ideally should have a uniform distribution of visibility pixel values. Based on this, the probability distribution of visibility values for the object and reference data was plotted (Figure 5.12, bottom). The top row of this figure displays the 2D visibility maps for the object (left) and reference (right) data. Under the assumption of homogeneous reference visibility, the two lowest bins in its probability distribution (right bottom subplot) were identified as noise and subsequently removed. The pixel values falling within these removed ranges were then replaced using interpolation method 1. This method, which performs refilling through a global operation followed by local selection, was chosen for this specific case because it is particularly well-suited for acquiring uniformly distributed pixel values of the detector plane.

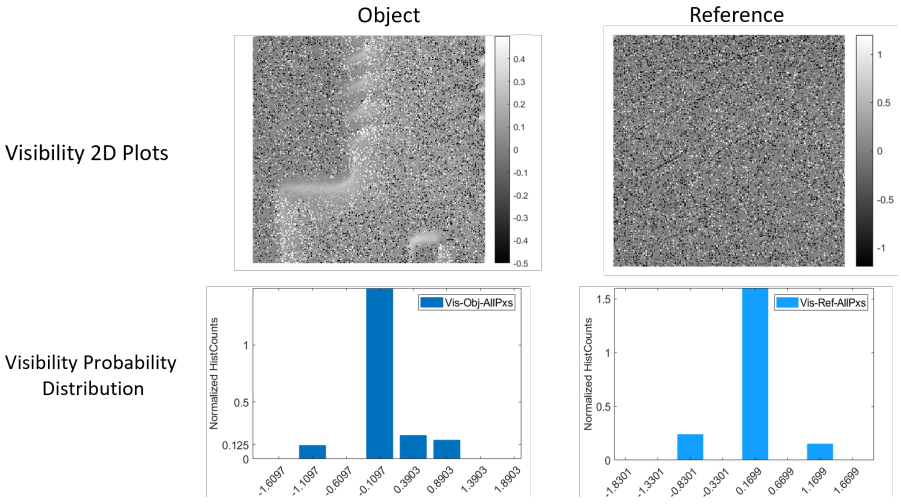

Figure 5.12: Visibility plot and probability distribution

The original and corrected visibility of the reference data are

shown in Figure 5.13. The correction resulted in a significantly darker visibility map, though, variations in the brightness of some pixels remain apparent within a small range.

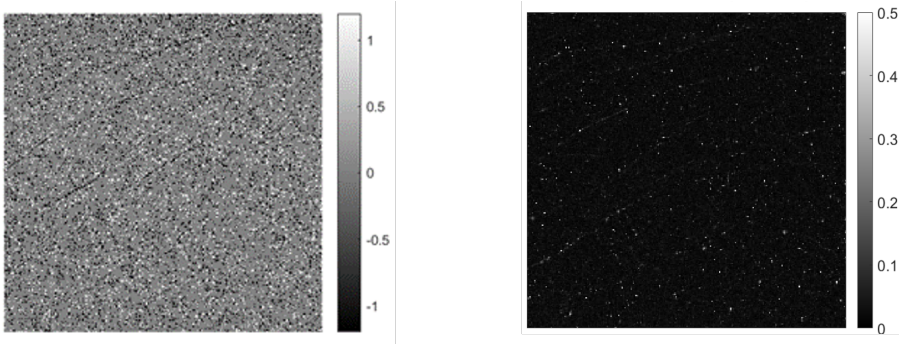

Figure 5.13: visibility correction. The left side shows the original visibility values of the reference data of measurement II, where the right side is the optimized visibility map.

5.3.3 Comparison of Original and Optimized Dark-Field Images

Figure 5.14 presents a detailed comparison of the original and optimized dark-field images, showcasing the impact of different post-processing approaches across three distinct subplots.

Subplot a) illustrates the initial reconstruction of the dark-field image, derived directly from the fitting results of Eq-II without any subsequent optimization or noise reduction techniques. As such, it serves as a baseline, representing the raw output of the reconstruction algorithm before any refinement. This image typically contains inherent noise and artifacts that are not mitigated by the initial fitting process.

Subplot b), in contrast, displays the result of the first optimization method applied. This approach combines a goodness-of-fit (GoF) threshold of 0.5 with interpolation method 1. The appli-

cation of this threshold helps to filter out less reliable pixel data, while interpolation method 1 subsequently repaints the empty or rejected pixels. This combination aims to enhance image quality by selectively preserving robust signals and intelligently filling in missing information, leading to an improved visual representation of the dark-field signal.

Subplot c) showcases the outcome of the second optimization method. This advanced technique relies on evaluating the correctness of the visibility of the reference data by analyzing its probability distribution. This method is conceptually distinct from the first, focusing on a more fundamental property of the interferometric signal. The goal here is to refine the image based on a statistical understanding of the signal's quality, leading to a potentially more accurate and robust reconstruction.

Upon visual inspection, both optimization approaches independently contribute to the improvement of the dark-field images from the baseline. However, method two consistently demonstrates a clearer advantage in enhancing the thread line edge signal, yielding sharper and more defined features compared to method one. This suggests a superior ability to differentiate the object's boundaries from the surrounding background and noise.

Despite its enhanced performance for dark-field images, it is important to note that optimization method two, which is based on the visibility probability distribution, is unlikely to be suitable for phase contrast images. This limitation stems from the inherent potential for spatial variation of the reference data's phase shift

across the detector area. Such variations are typically dependent on the wavefront properties of the X-ray beam, and if not accurately accounted for, they can introduce artifacts or inaccuracies when applying a visibility-based optimization approach to phase contrast data. This distinct behavior highlights the modality-specific challenges in X-ray interferometric imaging.

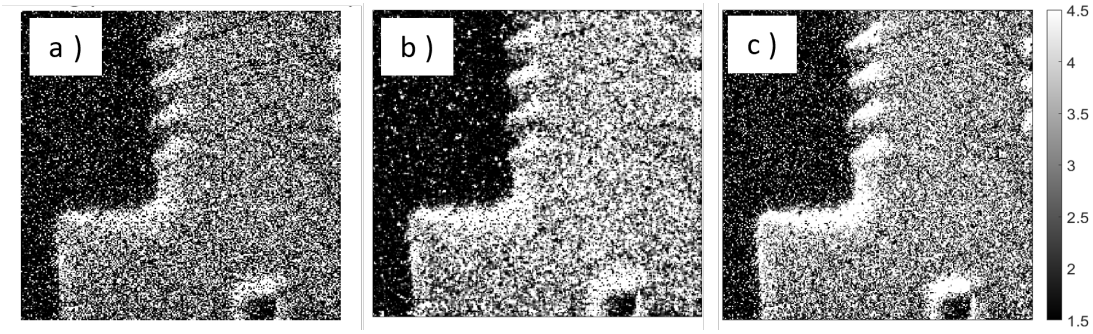

Figure 5.14: DF images reconstructed based on fitting Eq-II, a) without any optimization method, b) optimization one - combination of selection pixels with goodness of fitting as 0.5 followed by interpolation method 2, and c) optimization two - corrected visibility of reference data, utilizing probability distribution study

6

Summary and Outlook

6.1 Experiment Protocal Suggestion

As detailed in Subsection 4.2.2, optimizing detector positioning in conjunction with data processing is crucial for robust experimental design. Achieving high image visibility necessitates detector placement that accounts for precise energy determination and accurate fractional Talbot distance (frTD) calculation. For instance, since phase contrast images benefit from data within the bin of interest (BoI), both dark-field and phase contrast modalities can achieve superior image quality by utilizing BoI data with the detector positioned at the standard frTDa distance specifically determined by the phase grating's design energy.

6.2 Dark-field Image Reconstruction and Optimization

For the generation of Fourier series coefficients within the phase-stepping procedure, employing Eq-II is the recommended strategy to obtain high-quality dark-field images. This equation is particularly well-suited for extracting the subtle signal variations that contribute to the dark-field contrast, which is sensitive to microstructures

within the sample.

While it might seem intuitive to carefully select the photon energy spectrum for bin of interest (BoI) to match the intended design energy of the interferometer, this step is not essential. Moreover, in scenarios where the photon flux from the X-ray source is limited, strictly adhering to the design energy might lead to a significant reduction in the number of detected photons, potentially degrading the overall signal-to-noise ratio.

The dark-field images obtained using the proposed compact X-ray imaging system can be significantly improved through the application of the two optimization approaches thoroughly described in Chapter 5 of this thesis. These methods offer complementary ways to enhance the visibility of scattering features and reduce noise artifacts present in the raw reconstructed images.

Other than those presented in this thesis, approaches involving geometry and system parameter optimization may be combined with application-dependent optimization. Specifically, with biological test objects (involving, e.g., breast microcalcifications, microstructures of the lung alveoli, etc.), further crucial parameters to optimise for visibility enhancement could combine the autocorrelation length factor, which is an indicator of the length scale of microstructures that could be imaged with a given system, in conjunction with the considerations for radiation dose constraints. When considering optimization towards such application-dependent scenarios, the reliance of dark-field visibility on the autocorrelation length provides an additional mode of optimization that can be combined with

the methods presented in this thesis, which may allow tuning for selective imaging of specific structures in the case of polychromatic setups.

For radiation dose-based optimization of the dark-field approach described in this thesis, the trade-off between dose and visibility remains to be compared across the scenarios involving sample-before-grating and grating-before-sample geometries. The suitability of the proposed imaging approach within this thesis towards biological test objects remains to be seen, for instance, further quantitative investigation is required with well-characterized structures to identify suitable (visible) microstructural features, changes, and working ranges relevant to biological subjects.

6.3 Phase Contrast Image Improvement

The sharper object-air edges observed in the phase contrast images of Figure 3.4b) compared to Figure 3.5 (where only the curve-fitting setting varied) indicate a promising avenue for enhancing phase contrast imaging with the proposed compact setup. Specifically, treating the pattern period (p_t) as a constant during Fourier series coefficient curve-fitting appears to yield significant improvements.

Despite the inherent challenge of acquiring high-quality air-object interface phase contrast images with our compact setupprimarily due to beam coherence limitationsa viable alternative strategy involves combining the filtering of poorly fitted pixels (via a goodness-of-fit threshold during Fourier series generation) with subsequent interpolation. Future research will concentrate on determining opti-

mal thresholds for various experimental parameters and evaluating diverse interpolation methods.

Bibliography

[1] M. Berger, Q. Yang, and A. Maier, "Medical imaging systems. chapter 7: X-ray imaging," *Medical Imaging Systems: An Introductory Guide*, pp. 119–145, 2018.

[2] J. T. Bushberg and J. M. Boone, *The essential physics of medical imaging*. Lippincott Williams & Wilkins, 2011.

[3] M. A. Flower, *Webb's physics of medical imaging*. CRC press, 2012.

[4] W. C. Röntgen, "On a new kind of rays," *Science*, vol. 3, no. 59, pp. 227–231, 1896.

[5] T. Zhou, U. Lundström, T. Thüring, S. Rutishauser, D. H. Larsson, M. Stampanoni, C. David, H. Hertz, and A. Burvall, "Comparison of two x-ray phase-contrast imaging methods with a microfocus source," *Optics express*, vol. 21, no. 25, pp. 30 183–30 195, 2013.

[6] A. Bravin, P. Coan, and P. Suortti, "X-ray phase-contrast imaging: from pre-clinical applications towards clinics," *Physics in Medicine & Biology*, vol. 58, no. 1, p. R1, 2012.

[7] K. Scherer, E. Braig, S. Ehn, J. Schock, J. Wolf, L. Birnbacher, M. Chabior, J. Herzen, D. Mayr, S. Grandl *et al.*, "Improved

diagnostics by assessing the micromorphology of breast calcifications via x-ray dark-field radiography," *Scientific reports*, vol. 6, no. 1, p. 36991, 2016.

[8] S. Grandl, K. Scherer, A. Sztrókay-Gaul, L. Birnbacher, K. Willer, M. Chabior, J. Herzen, D. Mayr, S. D. Auweter, F. Pfeiffer *et al.*, "Improved visualization of breast cancer features in multifocal carcinoma using phase-contrast and dark-field mammography: an ex vivo study," *European radiology*, vol. 25, pp. 3659–3668, 2015.

[9] A. Ritter, G. Anton, F. Bayer, K. Gödel, G. Pelzer, J. Rieger, T. Weber, A. Zang, and T. Michel, "Simulation of dark-field imaging of micro-calcifications in human breast tissue with x-ray talbot-lau interferometry," *Journal of Instrumentation*, vol. 9, no. 05, p. C05028, 2014.

[10] J. Emons, P. A. Fasching, M. Wunderle, F. Heindl, J. Rieger, F. Horn, G. Pelzer, A. Ritter, T. Weber, M. Radicke *et al.*, "Assessment of the additional clinical potential of x-ray dark-field imaging for breast cancer in a preclinical setup," *Therapeutic advances in medical oncology*, vol. 12, p. 1758835920957932, 2020.

[11] K. Hellbach, F. G. Meinel, T. M. Conlon, K. Willer, A. Yaroshenko, A. Velroyen, M. Braunagel, S. Auweter, M. F. Reiser, O. Eickelberg *et al.*, "X-ray dark-field imaging to depict acute lung inflammation in mice," *Scientific reports*, vol. 8, no. 1, p. 2096, 2018.

[12] R. Gradl, K. Morgan, M. Dierolf, C. Jud, L. Hehn, B. Günther, W. Möller, D. Kutschke, L. Yang, T. Stoeger *et al.*, "Dynamic in vivo chest x-ray dark-field imaging in mice," *IEEE transactions on medical imaging*, vol. 38, no. 2, pp. 649–656, 2018.

[13] F. T. Gassert, T. Urban, M. Frank, K. Willer, W. Noichl, P. Buchberger, R. Schick, T. Koehler, J. von Berg, A. A. Fingerle *et al.*, "X-ray dark-field chest imaging: qualitative and quantitative results in healthy humans," *Radiology*, vol. 301, no. 2, pp. 389–395, 2021.

[14] K. Willer, A. A. Fingerle, L. B. Gromann, F. De Marco, J. Herzen, K. Achterhold, B. Gleich, D. Muenzel, K. Scherer, M. Renz *et al.*, "X-ray dark-field imaging of the human lunga feasibility study on a deceased body," *PloS one*, vol. 13, no. 9, p. e0204565, 2018.

[15] K. Willer, A. A. Fingerle, W. Noichl, F. De Marco, M. Frank, T. Urban, R. Schick, A. Gustschin, B. Gleich, J. Herzen *et al.*, "X-ray dark-field chest imaging for detection and quantification of emphysema in patients with chronic obstructive pulmonary disease: a diagnostic accuracy study," *The Lancet Digital Health*, vol. 3, no. 11, pp. e733–e744, 2021.

[16] K. Willer, A. Fingerle, W. Noichl, F. De Marco, M. Frank, T. Urban, R. Schick, A. Gustschin, B. Gleich, J. Herzen *et al.*, "X-ray dark-field chest imaging can detect and quantify emphysema in copd patients," *medRxiv*, pp. 2021–01, 2021.

[17] B. K. Fields, N. L. Demirjian, H. Dadgar, and A. Gholamrezanezhad, "Imaging of covid-19: Ct, mri, and pet," in *Seminars in Nuclear Medicine*, vol. 51, no. 4. Elsevier, 2021, pp. 312–320.

[18] H. Hatabu, Y. Ohno, W. B. Gefter, G. Parraga, B. Madore, K. S. Lee, T. A. Altes, D. A. Lynch, J. R. Mayo, J. B. Seo *et al.*, "Expanding applications of pulmonary mri in the clinical evaluation of lung disorders: Fleischner society position paper," *Radiology*, vol. 297, no. 2, pp. 286–301, 2020.

[19] M. Ando, R. Gupta, A. Iwakoshi, J.-K. Kim, D. Shimao, H. Sugiyama, N. Sunaguchi, T. Yuasa, and S. Ichihara, "X-ray dark-field phase-contrast imaging: Origins of the concept to practical implementation and applications," *Physica Medica*, vol. 79, pp. 188–208, 2020.

[20] J. R. Haaga and D. Boll, *Computed tomography & magnetic resonance imaging of the whole body e-book*. Elsevier Health Sciences, 2016.

[21] J. Vignero, "Exploration of clinical applications of talbot-lau interferometry," Ph.D. dissertation, Katholieke Universiteit Leuven, 2018.

[22] D. Paganin, *Coherent X-Ray Optics: Applications of the Phase-Space Representation. (Chapter 6: Propagation-Based Imaging)*. Oxford University Press, 2006, no. 6.

[23] R. Fitzgerald, "Phase-sensitive x-ray imaging," *Physics today*, vol. 53, no. 7, pp. 23–26, 2000.

[24] S. Tao, C. He, X. Hao, C. Kuang, and X. Liu, "Principles of different x-ray phase-contrast imaging: a review," *Applied Sciences*, vol. 11, no. 7, p. 2971, 2021.

[25] J. Keyriläinen, A. Bravin, M. Fernández, M. Tenhunen, P. Virkkunen, and P. Suortti, "Phase-contrast x-ray imaging of breast," *Acta radiologica*, vol. 51, no. 8, pp. 866–884, 2010.

[26] T. Weitkamp, C. David, O. Bunk, J. Bruder, P. Cloetens, and F. Pfeiffer, "X-ray phase radiography and tomography of soft tissue using grating interferometry," *European journal of radiology*, vol. 68, no. 3, pp. S13–S17, 2008.

[27] S. Wilkins, T. E. Gureyev, D. Gao, A. Pogany, and A. Stevenson, "Phase-contrast imaging using polychromatic hard x-rays," *Nature*, vol. 384, no. 6607, pp. 335–338, 1996.

[28] F. Pfeiffer, M. Bech, O. Bunk, P. Kraft, E. F. Eikenberry, C. Brönnimann, C. Grünzweig, and C. David, "Hard-x-ray dark-field imaging using a grating interferometer," *Nature materials*, vol. 7, no. 2, pp. 134–137, 2008.

[29] L. Quenot, S. Bohic, and E. Brun, "X-ray phase contrast imaging from synchrotron to conventional sources: A review of the existing techniques for biological applications," *Applied Sciences*, vol. 12, no. 19, p. 9539, 2022.

[30] T. Tuohimaa, M. Otendal, and H. M. Hertz, "Phase-contrast x-ray imaging with a liquid-metal-jet-anode microfocus source," *Applied Physics Letters*, vol. 91, no. 7, 2007.

[31] K. Shaker, I. Häggmark, J. Reichmann, M. Arsenian-Henriksson, and H. M. Hertz, "Phase-contrast x-ray tomography resolves the terminal bronchioles in free-breathing mice," *Communications Physics*, vol. 4, no. 1, p. 259, 2021.

[32] M. Krenkel, M. Töpperwien, M. Bartels, P. Lingor, D. Schild, and T. Salditt, "X-ray phase contrast tomography from whole organ down to single cells," in *Developments in X-Ray Tomography IX*, vol. 9212. SPIE, 2014, pp. 186–198.

[33] M. S. Nielsen, T. Lauridsen, M. Thomsen, T. Jensen, M. Bech, L. Christensen, E. Olsen, M. Hviid, R. Feidenhans, and F. Pfeiffer, "X-ray tomography using the full complex index of refraction," *Physics in Medicine & Biology*, vol. 57, no. 19, p. 5971, 2012.

[34] M. Bech, O. Bunk, T. Donath, R. Feidenhans, C. David, and F. Pfeiffer, "Quantitative x-ray dark-field computed tomography," *Physics in Medicine & Biology*, vol. 55, no. 18, p. 5529, 2010.

[35] B. K. Blykers, C. Organista, M. N. Boone, M. Kagias, F. Marone, M. Stampanoni, T. Bultreys, V. Cnudde, and J. Aelterman, "Tunable x-ray dark-field imaging for sub-resolution

feature size quantification in porous media," *Scientific reports*, vol. 11, no. 1, p. 18446, 2021.

[36] M. Ando, K. Yamasaki, F. Toyofuku, H. Sugiyama, C. Ohbayashi, G. Li, L. Pan, X. Jiang, W. Pattanasiriwisawa, D. Shimao *et al.*, "Attempt at visualizing breast cancer with x-ray dark field imaging," *Japanese journal of applied physics*, vol. 44, no. 4L, p. L528, 2005.

[37] P. Guo, L. Zhang, J. Lu, H. Zhang, X. Zhu, C. Wu, X. Zhan, H. Yin, Z. Wang, Y. Xu *et al.*, "Grating-based x-ray dark-field ct for lung cancer diagnosis in mice," *European Radiology Experimental*, vol. 8, no. 1, p. 12, 2024.

[38] L. Heck, M. Dierolf, C. Jud, E. Eggl, T. Sellerer, K. Mechlem, B. Günther, K. Achterhold, B. Gleich, S. Metz *et al.*, "Contrast-enhanced spectral mammography with a compact synchrotron source," *PLoS One*, vol. 14, no. 10, p. e0222816, 2019.

[39] B. Hornberger, J. Kasahara, M. Gifford, R. Ruth, and R. Loewen, "A compact light source providing high-flux, quasi-monochromatic, tunable x-rays in the laboratory," in *Advances in Laboratory-based X-Ray Sources, Optics, and Applications VII*, vol. 11110. SPIE, 2019, p. 1111003.

[40] N. Rīgere, M. Wurzer, M. Dierolf, B. Günther, F. Pfeiffer, and R. Kienberger, "Laboratory-scale production of tunable, narrow-bandwidth x-rays in the clinical energy regime," in *Frontiers in Ultrafast Optics: Biomedical, Scientific, and*

Industrial Applications XXV, vol. 13353. SPIE, 2025, p. 1335302.

[41] A. Yan, X. Wu, and H. Liu, "Quantitative theory of x-ray interferometers based on dual phase grating: fringe period and visibility," *Optics Express*, vol. 26, no. 18, pp. 23 142–23 155, 2018.

[42] ——, "Predicting fringe visibility in dual-phase grating interferometry with polychromatic x-ray sources," *Journal of X-ray Science and Technology*, vol. 28, no. 6, pp. 1055–1067, nov 2020. [Online]. Available: https://content.iospress.com/articles/journal-of-x-ray-science-and-technology/xst200747

[43] Y. Ge, J. Ma, Z. Li, H. Li, F. Zhang, and Z. Peng, "Dual phase grating based x-ray differential phase contrast imaging with source grating: theory and validation," *Optics Express*, vol. 28, no. 7, pp. 9786–9801, apr 2020. [Online]. Available: https://opg.optica.org/oe/abstract.cfm?uri=oe-28-7-9786

[44] M. Kagias, I. Zanette, T. Weitkamp, and C. David, "Dual phase grating interferometer for tunable dark-field sensitivity," *Applied Physics Letters*, vol. 110, no. 1, p. 011106, jan 2017. [Online]. Available: https://doi.org/10.1063/1.4972535

[45] J. Yang, Z. Li, J. Ma, Y. Ge, F. Zhang, and Z. Peng, "Analysis of period and visibility of dual phase grating interferometer," *Chinese Physics B*, vol. 31,

no. 5, p. 058701, may 2022. [Online]. Available: https://iopscience.iop.org/article/10.1088/1674-1056/ac516c

[46] R. Tang, Z. Li, J. Ma, Y. Ge, F. Zhang, and Z. Peng, "Detailed analysis of the interference patterns measured in lab-based x-ray dual-phase grating interferometry through wave propagation simulation," *Optics Express*, vol. 31, no. 2, pp. 1677–1691, jan 2023. [Online]. Available: https://opg.optica.org/oe/abstract.cfm?uri=oe-31-2-1677

[47] S. Rutishauser. (2013) X-ray grating interferometry for imaging and metrology. [Online]. Available: https://www.research-collection.ethz.ch/handle/20.500.11850/16/discover

[48] J. A. Seibert and J. M. Boone, "X-ray imaging physics for nuclear medicine technologists. part 2: X-ray interactions and image formation," *Journal of nuclear medicine technology*, vol. 33, no. 1, pp. 3–18, 2005.

[49] W. SW, "Phase-contrast imaging using polychromatic hard x-rays," *Nature*, vol. 384, pp. 335–338, 1996.

[50] A. Snigirev, I. Snigireva, V. Kohn, S. Kuznetsov, and I. Schelokov, "On the possibilities of x-ray phase contrast microimaging by coherent high-energy synchrotron radiation," *Review of scientific instruments*, vol. 66, no. 12, pp. 5486–5492, 1995.

[51] T. Weitkamp, A. Diaz, C. David, F. Pfeiffer, M. Stampanoni, P. Cloetens, and E. Ziegler, "X-ray phase imaging with a

grating interferometer," *Optics express*, vol. 13, no. 16, pp. 6296–6304, 2005.

[52] J. Herzen, "A grating interferometer for materials science imaging at a second-generation synchrotron radiation source," Ph.D. dissertation, Staats-und Universitätsbibliothek Hamburg Carl von Ossietzky, 2010.

[53] T. Thüring, "Compact X-ray grating interferometry for phase and dark-field computed tomography in the diagnostic energy range," Ph.D. dissertation, Eidgenössische Technische Hochschule Zürich, 2013.

[54] M.-C. Zdora, *X-ray phase-contrast imaging using near-field speckles*. Springer Nature, 2021.

[55] F. Pfeiffer, T. Weitkamp, O. Bunk, and C. David, "Phase retrieval and differential phase-contrast imaging with low-brilliance x-ray sources," *Nature physics*, vol. 2, no. 4, pp. 258–261, 2006.

[56] P. Carré, "Installation et utilisation du comparateur photoélectrique et interférentiel du bureau international des poids et mesures," *Metrologia*, vol. 2, no. 1, p. 13, 1966.

[57] J. H. Bruning, D. R. Herriott, J. E. Gallagher, D. P. Rosenfeld, A. D. White, and D. J. Brangaccio, "Digital wavefront measuring interferometer for testing optical surfaces and lenses," *Applied optics*, vol. 13, no. 11, pp. 2693–2703, 1974.

[58] M. Bech, "X-ray imaging with a grating interferometer phd thesis," *University of Copenhagen, Denmark*, 2009.

[59] J. M. Cowley, *Diffraction physics*. Elsevier, 1995.

[60] C.-L. Chen, Y. Wang, J. J. Lee, and B. M. Tsui, "Integration of simset photon history generator in gate for efficient monte carlo simulations of pinhole spect," *Medical physics*, vol. 35, no. 7Part1, pp. 3278–3284, 2008.

[61] D. Sarrut, M. Bardiès, N. Boussion, N. Freud, S. Jan, J. M. Létang, and G. Loudos, "A review of the use and and potential of the GATE Monte Carlo simulation code for radiation therapy and dosimetry applications," *Medical Physics*, vol. 41, no. 6, p. 064301, 2014.

[62] OpenGATE Collaboration. Introduction — opengate. [Online]. Available: https://opengate.readthedocs.io/en/latest/introduction.html#

[63] M. Langer, Z. Cen, S. Rit, and J. M. Létang, "Towards monte carlo simulation of x-ray phase contrast using gate," *Optics express*, vol. 28, no. 10, pp. 14 522–14 535, 2020.

[64] A. Velroyen, "X-ray phase-contrast and dark-field imaging of small animals: Contrast enhancement and in vivo imaging," Ph.D. dissertation, Technische Universität München, 2015.

[65] John D'Errico. (2006, Apr.) Inpaint-nans: in-paints over nans in an array. [Online]. Available: https://code.usgs.gov/wma/osd/trivia/-/blob/main/code/inpaint_nans.m

[66] A. Konijnenberg and Urbach, "Chapter 6.07: Fresnel and fraunhofer approximations." [Online]. Available: https://phys.libretexts.org/Bookshelves/Optics/BSc_Optics_(Konijnenberg_Adam_and_Urbach)/06%3A_Scalar_diffraction_optics/6.07%3A_Fresnel_and_Fraunhofer_Approximations

A

Appendix

A.1 Paraxial Fresnel Diffraction

Transmission function of grating

As demonstrated in Chapter 4.1 of Thuering's dissertation [53], the Talbot interference pattern can be mathematically modeled by the convolution of the transmission function T(x,y;z=0) of a phase grating (G1) and the Fresnel propagator P(x,y,z). For a one-direction (1D) grating with a pitch width of p_1 and a 0.5 duty cycle causing a φ phase shift to a plane wave, the transmission function T in one pitch range p_1 can be simplified to T(x;z=0) and is represented as follows:

$$T(x) = \begin{cases} e^{i\phi}, & \text{for } x \in [-p_1/2, 0] \\ 1, & \text{for } x \in [0, p_1/2] \end{cases} \tag{A.1}$$

where notably, $\phi = \pi/2$ while the grating is illuminated by a monochromatic beam at 37.5 keV, due to the phase grating utilized in this PhD work.

Given that the grating is a periodic object with a fundamental

period p_1, its overall transmission function $T(x)$ over the entire grating with a width of N times p_1 can be represented by

$$T(x + Np_1) = T(x), N = 1, 2, 3... \tag{A.2}$$

As a periodic function, it can be expressed as a Fourier series

$$T(x) = \sum_{n=-\infty}^{\infty} c_n e^{i\frac{2\pi nx}{p_1}} \tag{A.3}$$

here C_n, representing the amplitude of n^{th} harmonic, are the Fourier coefficients determined by

$$c_n = \frac{1}{p_1} \int_{-p_1/2}^{p_1/2} T(x) e^{-i\frac{2\pi nx}{p_1}} \, dx \tag{A.4}$$

Paraxial approximation

To define a wave filed, the propagated distance r from source plane (x',y',0) to image plane (x,y,z) is calculated by

$$r^2 = (x - x')^2 + (y - y')^2 + z^2 \tag{A.5}$$

And, the relative radius ρ can be written as

$$\rho = \sqrt{(x - x')^2 + (y - y')^2} \tag{A.6}$$

Rewrite propagating distance as

$$r = \sqrt{\rho^2 + z^2} = z\sqrt{1 + \rho^2/z^2} \tag{A.7}$$

Recalling binomial expansion,

$$r/z = 1 + \frac{1}{2}\frac{\rho^2}{z^2} - \frac{1}{8}(\frac{\rho^2}{z^2})^2 + ... \tag{A.8}$$

With paraxial approximation, we have

$$\rho \ll r \tag{A.9}$$

Therefore,

$$r \approx z + \frac{\rho^2}{2z} + ... \tag{A.10}$$

Fresnel propagator under paraxial approximation

As the interference pattern is the 2D intensity distribution of diffracted waves downstream of phase grating, the wave field follows Fresnel diffraction [47,53,66], where the paraxial Fresnel propagator is called and can be written as

$$P(x, y, z) = \frac{1}{i\lambda z} e^{ik(z + \frac{(x^2+y^2)}{2z})} = \frac{e^{ikz}}{i\lambda z} e^{i\frac{k}{2z}(x^2+y^2)} \tag{A.11}$$

Notably, the propagator vector r is substituted by Eq. A.10, instead of Eq. A.7.

Given that $k = 2\pi/\lambda$ is the wave number and λ is the wavelength of the illuminating beam, the propagator function can be simplified for a 1D grating as follows

$$P(x, z) = \frac{e^{ikz}}{i\lambda z} e^{i\frac{k}{2z}(x^2)} \tag{A.12}$$

Mathematically, the resulting wave field $E(x, z)$ is determined by the convolution of the transmission function and the propagator

function, such that

$$E(x,z) = T(x) \otimes P(x,z) \tag{A.13}$$

Applying the Fourier transform $\mathcal{F}$ and its inverse $\mathcal{F}^{-1}$, the expression A.13 can be rewritten as

$$E(x,z) = \mathcal{F}^{-1}\{\mathcal{F}\{T(x)\} \cdot \mathcal{F}\{P(x,z)\}\} \tag{A.14}$$

At a certain propagating distance, z can be treated as a constant, therefore, the e^{ikz} constant phase can be ignored for deriving the wave field along the x direction at this distance. Consequently, Fourier transform of the Fresnel propagator along the x direction $\mathcal{F}\{P(x, z = cons)\}$ can be expressed as

$$\mathcal{F}\left\{e^{i\frac{k}{2z}x^2}\right\} = \sqrt{\frac{2\pi z}{k}} e^{i\frac{\pi}{4}} e^{-i\frac{z}{2k}(2\pi f_x)^2} \tag{A.15}$$

where f_x is the spatial frequency. While Substituting $k = 2\pi/\lambda$, the Fourier transform $\mathcal{F}\{P(x)\}$ is

$$\mathcal{F}\{P(x)\} = \mathcal{F}\left\{e^{i\frac{k}{2z}x^2}\right\} \propto e^{-i\pi\lambda z f_x^2} \tag{A.16}$$

Fourier domain

While substituting Eq. A.3 and Eq. A.16 into Eq. A.13, the convolution of transmission function $T(x)$ and Fresnel propagator $P(x)$ can be acquired by production in Fourier domain, as

$$\mathcal{F}\{E(x,z)\} = \left(\sum_{m=-\infty}^{\infty} c_m \delta\left(f_x - \frac{m}{p}\right)\right) \cdot \left(\text{constant} \cdot e^{-i\pi\lambda z f_x^2}\right) \tag{A.17}$$

For each Fourier component m, the delta function defines

$$f_x = m/p \tag{A.18}$$

Therefore

$$\mathcal{F}\{E(x,z)\}_m \propto c_m e^{-i\pi\frac{\lambda z m^2}{p^2}} \tag{A.19}$$

To get back to the wave field, the reverse discrete Fourier transform is needed, as

$$E(x,z) = \sum_{m=-\infty}^{\infty} c_m e^{-i\pi\frac{\lambda z m^2}{p^2}} e^{i2\pi m x/p} \tag{A.20}$$

Self-imaging and Talbot distance

The Talbot effect reveals the grating structure at a specific propagation distance z_t, where the resulting wave field $E(x, z_t)$ is equivalent to the grating transmission function $T(x; z = 0)$, which can be presented as

$$E(x; z = z_t) = \mathcal{F}^{-1}\{\mathcal{F}\{T(x)\} \cdot \mathcal{F}\{P(x, z_t)\}\} = T(x) \tag{A.21}$$

By comparing Eq. A.20 and A.3, the condition of Eq. A.21 can be fulfilled only if the phase factor $e^{-i\pi\frac{\lambda z_T m^2}{p^2}}$ appears to be unity, leading to a constant overall phase factor for all m.

$$e^{-i\pi\frac{\lambda z_T m^2}{p^2}} = 1 \tag{A.22}$$

This condition is met when the exponent is an integer multiple of 2π:

$$-\pi\frac{\lambda z_T m^2}{p^2} = -2\pi N_m \tag{A.23}$$

(where N_m is an integer that depends on m)

$$\frac{\lambda z_T m^2}{p^2} = 2N_m \tag{A.24}$$

This equation must hold for all m. The simplest integer N_m that satisfies this for all m is when $N_m = m^2 N_0$ for some integer N_0. The smallest non-zero N_0 that makes this work for all m simultaneously is $N_0 = 1$. So, for $m = 1$, $\frac{\lambda z_T}{p^2} = 2$. This gives the fundamental Talbot distance:

$$z_T = \frac{2p^2}{\lambda}$$

Therefore, the Talbot distance z_T is derived as

$$\frac{2p^2}{\lambda} \tag{A.25}$$

The equivalent conclusion of Talbot distance can also be derived by recalling Euler's formula here,

$$e^{-it} = \cos(t) - i\sin(t) \tag{A.26}$$

and substituting this for the phase factor, the condition for self-imaging becomes

$$\cos(t) - i\sin(t) = 1 \tag{A.27}$$

This equation is satisfied only when $sin(t) = 0$ and $cos(t) = 1$, which occurs when $t = 2m\pi$, where m is an integer. Now, equating t with the exponent of the phase factor, $\pi\frac{n^2 z_t \lambda}{p_1^2}$, the distance to the

nearest (m=1) self-image can be derived as:

$$z_t = \frac{2p_1^2}{\lambda} \tag{A.28}$$

A.2 Code Documentation

Phase-Stepping

```python
import numpy as np
import matplotlib.pyplot as plt
from scipy.optimize import curve_fit

def sine_function(x, A, B, C):
    """
    Defines a general sine function: I1 * sin(x + delta_phi) + I0
    where:
        A (I1): Amplitude
        B (I0): Offset (background)
        C (delta_phi): Phase shift
    """
    return A * np.sin(x + C) + B

from matplotlib.ticker import Formatter
class PiMultipleFormatter(Formatter):
    def __call__(self, x, pos=None):
        if x == 0:
            return "0"
        quotient = x / np.pi
        if quotient == 1:
            return "$\pi$"
        elif quotient == -1:
            return "$-\pi$"
        elif quotient == 0.5:
            return "$\pi/2$"
        elif quotient == -0.5:
            return "$-\pi/2$"
        elif quotient == 1.5:
            return "$3\pi/2$"
        elif quotient == -1.5:
            return "$-3\pi/2$"
```

```
        else:
            return f"${quotient:.0f}\pi$"

if __name__ == '__main__':
    true_amplitude = 2.5
    true_offset = 1.0
    true_phase_shift = np.pi / 4
    phase_steps_fine = np.linspace(0, 2 * np.pi, 100)
    true_intensity = sine_function(phase_steps_fine, true_amplitude, true_offset, true_phase_shift)

    num_samples = 5
    sampled_phase_steps = np.linspace(0, 2 * np.pi * (num_samples - 1) / num_samples, num_samples)
    sampled_intensity = sine_function(sampled_phase_steps, true_amplitude, true_offset, true_phase_shift) + 0.1 * np.random.randn(num_samples)

    initial_guess = [1.0, 2.0, 0.0]

    try:
        popt, pcov = curve_fit(sine_function, sampled_phase_steps, sampled_intensity, p0=initial_guess)
        fitted_amplitude, fitted_offset, fitted_phase_shift = popt
        fitted_intensity = sine_function(phase_steps_fine, fitted_amplitude, fitted_offset, fitted_phase_shift)
    except RuntimeError:
        print("Error: Optimal parameters not found.")
        exit()

    plt.figure(figsize=(8, 4))
    plt.scatter(sampled_phase_steps, sampled_intensity, color='red', marker='o', label=f'Sampled Intensities ({num_samples} points)')
    plt.plot(phase_steps_fine, fitted_intensity, 'b-', label='Fitted Sine Curve')
    plt.xlabel('Phase Step (radians)')
    plt.ylabel('Intensity')
    plt.title('Sine Curve Fitting from Sampled Intensities')
    plt.legend()
    plt.grid(True)
    plt.gca().xaxis.set_major_formatter(PiMultipleFormatter())
```

```
    plt.gca().xaxis.set_major_locator(plt.MultipleLocator(base=np.pi / 2))
    plt.tight_layout()
    plt.show()

    print("\n--- Fitted Parameters ---")
    print(f"Fitted Amplitude: {fitted_amplitude:.2f} (True: {true_amplitude:.2f})")
    print(f"Fitted Offset: {fitted_offset:.2f} (True: {true_offset:.2f})")
    print(f"Fitted Phase Shift: {fitted_phase_shift:.2f} (True: {true_phase_shift:.2f})")
```

Listing A.1: Sine curve fitting with sampled data

Talbot Carpet

```
clear all; clc
%%%%%%%%%%%% GRATING PARAMETERS AND THE REAL SPACE %%%%%%%%%%%%%%%%%%%%%%%%%%%%%%%%
Nz = 5500;          % number of field planes, i.e., pixels in Z-direction
z_range = 0.5e6;    % z_range, 0.5 m

G_real = 2.4;       % Grating period in ţm
phase = pi/2;       % pi/2  phase shift acquired in sections with width w

x_range_real = 4*G_real; % um, x-size of the world in multiples of G_real
y_range_real = 1;  % not used

%%%%%%%%%%%% INITIAL FIELD JUST AFTER THE GRATING %%%%%%%%%%%%%%%%%%%%%%%%%%%%%%%%
G = 80;             % Grating period in 'pixels'
w = 40;             % width of the phase-shifting section within one grating period
x_range = round(x_range_real/G_real*G);
y_range = y_range_real;

indc = ceil(x_range/2);
object = zeros(y_range,x_range);  % transverse field at the input plane
```

```
20
21 for j=-2:1
22     object(:,indc+j*G+1:indc+j*G+w) = exp(1i*phase);
23     object(:,indc+j*G+w+1:indc+j*G+G) = 1;
24 end
25
26 %%%%%%%%%%% SPATIAL FREQUENCIES, i.e., COORDINATES IN FOURIER SPACE
       %%%%%%%%%%%%%%%
27 k_x = (-floor(x_range/2):ceil(x_range/2)-1)*2*pi/x_range_real;
28 % k_y = (-floor(y_range/2):ceil(y_range/2)-1)*2*pi/y_range;
29 k_y = 0;
30
31 %% Mono
32 % PROPAGATION OF SCATTERED WAVEFRONT CALCULATED %%
33 L1 = "wavelength of mono-energy"; %37.5keV
34 k1 = 2*pi/L1;
35 intensity_xz_1 = zeros(x_range,Nz);
36 for ii = 1:Nz
37     z = (ii-1)*z_range/Nz; % convert 'pixel' of z-axis back to length
       um
38 for j = 1:y_range
39     for jj = 1:x_range
40         if ((k_x(jj))^2 + (k_y(j))^2 <= k1^2)
41             propagator1(j,jj) = exp(-1i*z*sqrt(k1^2 - (k_x(jj))^2 - (
       k_y(j))^2));
42         end
43     end
44 end
45 intensity1 = (abs(ifft2 (fftshift(fft2(object)).*propagator1))).^2;%
       dot product, A.*B=C, C(i,j)=A(i,j)*B(i,j)
46 intensity_xz_1(:,ii) = intensity1(ceil(y_range/2),:);
47 end
48 %%% PLOTTING THE INTENSITY OF THE PROPAGATED FIELD IN THE (X,Z)-PLANE
49 z_axis = linspace(0,z_range,Nz);
50 x_axis = ((1:x_range)-0.5*x_range)*G_real/G;
51 z_T1 = 2*G_real^2/L1;% Talbot distance only depend on wavelength and
       grating period
52 z_fT1 = 3*z_T1/4; % third fractional talbot distance
53
54 pattern_frTD = intensity_xz_1(:,round(z_fT1*Nz/z_range)+1);
55 pattern_TD = intensity_xz_1(:,round(z_T1*Nz/z_range)+1);
```

```
56
57 figure();
58 subplot(2,2,[1,2]),
59 colormap(gray);
60 imagesc(z_axis*1e-6,x_axis,intensity_xz_1);
61 title('Subplot 1: Talbot Carpet of \pi / 2 - shifting Phase Grating
      of 37.5 keV Photon Energy','FontSize',14);
62 xlabel('Propagation Distance, z [m]','FontSize',14)
63 ylabel('')
64 set(gca,'ytick',[]) % --> commond for removing y-axis
65 colormap(gray);%colormap(hot)
66 hold on
67 plot([z_T1,z_T1]*1e-6,[x_axis(1),x_axis(end)],'y-')
68 hold on
69 plot([z_fT1,z_fT1]*1e-6,[x_axis(1),x_axis(end)],'g--')
70 legend('1st Talbot Distance','3rd Fractional Talbot Distance','
      FontSize',12,'textcolor','black','Location','southeast');
71 hold off
72
73 %% PROPAGATION OF SCATTERED WAVEFRONT CALCULATED BY ANGULAR SPECTRUM
      METHOD
74 clear propagator
75 lambda = [lambda_1, lambda_2,..., lambda_N"]; % list of Polychromatic
       Wavelength Component, size of N
76 k = zeros(1,size(lambda,2));
77 intensity_xz = zeros(x_range,Nz,size(lambda,2));
78 for m = 1:size(lambda,2)
79     k(m) = 2*pi/lambda(m);
80     for ii = 1:Nz
81         z = (ii-1)*z_range/Nz;
82         for j = 1:y_range
83             for jj = 1:x_range
84                 if ((k_x(jj))^2 + (k_y(j))^2 <= k(m)^2)
85                     propagator(j,jj,m) = exp(-1i*z*sqrt(k(m)^2 - (k_x
   (jj))^2 - (k_y(j))^2));
86                 end
87             end
88         end
89         intensity = (abs(ifft2 (fftshift(fft2(object)).*propagator
   (:,:,m)))).^2;
90         intensity_xz(:,ii,m) = intensity(ceil(y_range/2),:);
```

```
    end
end

%% Averaged Energy %%
prob_Avg = [1/N,...,1/N]; % Equally distributed probability of
    different wavelength components, the size N
multi_intensity_Avg = zeros(size(intensity_xz));
for np=1:size(prob_Avg,2)
    multi_intensity_Avg(:,:,np) = intensity_xz(:,:,np).*prob_Avg(np);
end
multi_intensity_1 = sum(multi_intensity_Avg, 3);

%% Effective Energy based on Weighted spectrum %%
prob_random = [p_1, p_2, ..., p_N]; % Aligned with the probability
    distribution of experimental spectrum, size N. Besides, p_i is the
     percentage of lambda_i. The sum of prob_random equals 1.
multi_intensity = zeros(size(intensity_xz));
for np=1:size(prob_random,2)
    multi_intensity(:,:,np) = intensity_xz(:,:,np).*prob_random(np);
end
intensity_multi = sum(multi_intensity, 3);

%% PLOTTING THE INTENSITY OF THE PROPAGATED FIELD IN THE (X,Z)-PLANE
    %%
L_meanEn = wavelength of effective energy; %lambda * prob_random';%
    effective energy of BoI; % 37.5keV
z_T_meanEn = 2*G_real^2/L_meanEn;
z_fT_meanEn = 3*z_T_meanEn/4;

pattern_frTD_Avg_multi = multi_intensity_1(:,round(z_fT_meanEn*Nz/
    z_range)+1);
pattern_frTD_Spec_multi = intensity_multi(:,round(z_fT_meanEn*Nz/
    z_range)+1); % of mean energy 37.5 keV

figure();
subplot(1,3,1);
imagesc(z_axis*1e-6, x_axis, multi_intensity_1);
xlabel('Propagation Distance, z [m]','FontSize',14)
ylabel('Equally Distributed Polychromatic Incident Beam','FontSize'
    ,14)
set(gca,'ytick',[])
```

```
subplot(1,3,2);
imagesc(z_axis*1e-6, x_axis, intensity_multi);
xlabel('Propagation Distance, z [m]','FontSize',14)
ylabel('Weighted Spectrum of Poly-Beam Eff-Energy 37.5 keV','FontSize
    ',14)
set(gca,'ytick',[]) % --> commond for removing y-axis
colormap(hot);%colormap(gray)
% sgtitle('Talbot Carpets of \pi / 2 - shifting Phase Grating','
    FontSize',16)
hold on
plot([z_fT_meanEn,z_fT_meanEn]*1e-6,[x_axis(1),x_axis(end)],'w--')
legend('3rd Fractional Talbot Distance of Effectiv Energy','FontSize'
    ,12,'textcolor','black','Location','southeast');
hold off
```

Listing A.2: MATLAB Code for Talbot Carpet Simulation

Fourier Coefficients Generation

```
nPosi = 7; repeat = 6;
lowEnergy = 5; highEnergy = 45; BinWidth = 0.01;
nBins = (highEnergy - lowEnergy)/BinWidth;
BoI_PS = 2980:4000; % Bin of interest selection for acquiring a
    preferred effective energy;
ROI_Row = (30:87); ROI_Col = (84:141);
pixels_ROI = numel(ROI_Row)*numel(ROI_Col); energy = linspace(
    lowEnergy,highEnergy,nBins);
pixels = 65536;

%% Read out reference data and object data %%
S = zeros(pixels,nBins,nPosi); % S can represent either reference or
    object date, depending on file
DataFiles = dir('D:\Experiments\...\Ref_ofSrew_Step_*.mat');
for i = 1:nPosi
  data = load(fullfile(DataFiles(i).folder, DataFiles(i).name));
  S(:,:,i)= data.px_bin_data;
end

spectrum_screw = squeeze(sum(S_screw,1)); % S_screw is the measured
    data of imaging object screw;
S_screw_BoI = S_screw(:,BoI_PS,:);
ave_S_screw_BoI = squeeze(mean(S_screw_BoI,3));
Image_screw_BoI = reshape(sum(ave_S_screw_BoI,2),256,256);
```

```
figure(), imagesc(Image_screw_BoI), title('screw of BoI');

counts_ave_screw_im3D = mean(S_screw,3);
Spec_ave_screw = sum(counts_ave_screw_im3D,1);
SpecStd_screw = std(spectrum_screw,0,2);
MeanEnergy_tpx_screw = sum(Spec_ave_screw.*energy)/sum(Spec_ave_screw);
MeanEnergy_BoI_tpx_screw = sum(Spec_ave_screw(BoI_PS).*energy(BoI_PS)) / sum(Spec_ave_screw(BoI_PS));
figure(), plot(energy,Spec_ave_screw), hold on
errorbar(energy(BoI_PS),Spec_ave_screw(BoI_PS)',SpecStd_screw(BoI_PS),'o'), hold off

spectrum_ref = squeeze(sum(S_ref,1)); % S_screw is the measured data of the imaging procedure without an object within the beam path;
S_ref_BoI = S_ref(:,BoI_PS,:);
ave_S_ref_BoI = squeeze(mean(S_ref_BoI,3));
Image_ref_BoI = reshape(sum(ave_S_ref_BoI,2),256,256);
figure(), imagesc(Image_ref_BoI), title('ref of BoI');

counts_ave_ref_im3D = mean(S_ref,3);
Spec_ave_ref = sum(counts_ave_ref_im3D,1);
SpecStd_ref = std(spectrum_ref,0,2);
MeanEnergy_tpx_ref = sum(Spec_ave_ref.*energy)/sum(Spec_ave_ref);
MeanEnergy_BoI_tpx_ref = sum(Spec_ave_ref(BoI_PS).*energy(BoI_PS)) / sum(Spec_ave_ref(BoI_PS));
figure(), plot(energy,Spec_ave_ref), hold on
errorbar(energy(BoI_PS),Spec_ave_ref(BoI_PS)',SpecStd_ref(BoI_PS),'o'), hold off

Image_screw_BoI_RoI = Image_screw_BoI(ROI_Row,ROI_Col);
Count_list_px_screw_RoI_BoI = reshape(Image_screw_BoI_RoI,pixels_ROI,1);
figure(), imagesc(Image_screw_BoI_RoI), title('screw RoI of BoI');

Obj_AllBins_PS = reshape(sum(S_screw,2),256,256,nPosi);
Ref_AllBins_PS = reshape(sum(S_ref,2),256,256,nPosi);
ObjRoI_AllBins_PS = Obj_AllBins_PS(ROI_Row,ROI_Col,:);
RefRoI_AllBins_PS = Ref_AllBins_PS(ROI_Row,ROI_Col,:);
ObjRoI_list = reshape(ObjRoI_AllBins_PS,3364,7);
RefRoI_list = reshape(RefRoI_AllBins_PS,3364,7);
```

```
55
56 Obj_BoI_PS = reshape(sum(S_screw_BoI,2),256,256,nPosi);
57 Ref_BoI_PS = reshape(sum(S_ref_BoI,2),256,256,nPosi);
58 ObjRoIBoI_list = reshape(Obj_BoI_PS(ROI_Row,ROI_Col,:),3364,7);
59 RefRoIBoI_list = reshape(Ref_BoI_PS(ROI_Row,ROI_Col,:),3364,7);
60
61
62 %%  Curve fitting for generating Fourier coefficients  %%
63 %%  capable of setting a threshold of goodness of fitting %%
64 x_obj = 0.0:0.8:4.8;
65 Obj = [step_obj_0 step_obj_1 step_obj_2 step_obj_3 step_obj_4
      step_obj_5 step_obj_6];
66 Ref = [step_ref_0 step_ref_1 step_ref_2 step_ref_3 step_ref_4
      step_ref_5 step_ref_6];
67 temp_table = {Obj; Ref};
68 coefficients0_Obj = zeros(size(Obj,1),4);
69 coefficients0_Ref = zeros(size(Ref,1),4);
70 figure()
71 if isequal(size(Obj,1),size(Ref,1))
72   for px = 1:size(Obj,1)
73     for data = 1:2
74       temp = temp_table{data}(px,:);
75       [fitresult, gof] = FourierFit(x_obj, temp);
76       if data==1
77         coefficients0_Obj(px,:) = gof.rsquare > 0 ? coeffvalues(
      fitresult) : NaN;
78       else
79         coefficients0_Ref(px,:) = gof.rsquare > 0 ? coeffvalues(
      fitresult) : NaN;
80       end
81     end
82     disp(['Pixel: ',num2str(px)])
83   end
84 else
85   disp('UNEQUAL SIZES FOR OBJECT AND REFERENCE')
86 end
87
88 %% Computation of signals of three image modalities %%
89 Att_Eq1_ThreeCoeffi_Allbins_index = 1 - coefficients0_Obj(:,3) ./
      coefficients0_Ref(:,3);
90 AttImg_THREETermsEq1 = reshape(Att_Eq1_ThreeCoeffi_Allbins_index
```

```
   ,256,256);
figure(), imagesc(AttImg_THREETermsEq1), colormap('gray'), title('
   Attenuation Eq1 3 Coefficients');

A1_O = sqrt(coefficients0_Obj(:,2).^2 + coefficients0_Obj(:,3).^2);
A1_R = sqrt(coefficients0_Ref(:,2).^2 + coefficients0_Ref(:,3).^2);
Vis_index = (A1_O./coefficients0_Obj(:,1)) ./ (A1_R./
   coefficients0_Ref(:,1));
VisImg = reshape(Vis_index,256,256);
figure(), imagesc(VisImg), colormap('gray'), title('Visibility Index
   Eq2');

Phi_obj = (2*pi)./coefficients0_Obj(:,1);
Phi_ref = (2*pi)./coefficients0_Ref(:,1);
Phase_diff = Phi_obj - Phi_ref;
```

Listing A.3: Experimental Data Processing and Fourier Coefficients Generation

Image Optimization

```
function [fitresult, gof] = myFit(xt, yt)
%CREATEFIT(XT,YT)
%  Create a fit.
%
%  Data for 'untitled fit 1' fit:
%      X Input : xt
%      Y Output: yt
%  Output:
%      fitresult : a fit object representing the fit.
%      gof : structure with goodness-of fit info.
%
%  See also FIT, CFIT, SFIT.

%  Auto-generated by MATLAB on 18-Oct-2023 20:37:40


%% Fit: 'untitled fit 1'.
[xData, yData] = prepareCurveData( xt, yt );

% Set up fittype and options.
%%  Eq-I %%
% ft = fittype( 'b1.*(cos(2*pi*x./b2 + 2*pi/b3)) + b4', 'independent
   ', 'x',
```

```
% 'dependent', 'y' ); % four terms of coefficients, Eq-I
%% Eq-II %%
% ft = fittype( 'b1.*(cos(2*pi*x./b2)) + b3.*(sin(2*pi*x./b2)) + b4',
    'independent', 'x',
% 'dependent', 'y' ); % four terms of coefficients, Eq-II

ft = fittype( 'b1.*(cos(x + 2*pi/b2)) + b3', 'independent', 'x', '
   dependent', 'y' );% three terms of coefficients
opts = fitoptions( 'Method', 'NonlinearLeastSquares' );
opts.Display = 'Off';
opts.StartPoint = [100 0.694828622975817 1000];

% Fit model to data.
[fitresult, gof] = fit( xData, yData, ft, opts );

% Plot fit with data.
% figure();
% h = plot( fitresult, xData, yData );
% legend( h, 'yt vs. xt', 'untitled fit 1', 'Location', 'NorthEast',
   'Interpreter', 'none' );
% % Label axes
% xlabel( 'xt', 'Interpreter', 'none' );
% ylabel( 'yt', 'Interpreter', 'none' );
% grid on
```

Listing A.4: Function of Fitting Equations, referring Eq-I and Eq-II

Declaration of Honor

I hereby declare that I produced this thesis independently and without prohibited external assistance, using only the listed references and tools. Throughout the development of this thesis, Artificial Intelligence (AI) tools were employed solely for grammar correction.

In the case of co-authorship, especially in the context of a cumulative dissertation, the own contribution is correctly and completely stated. I did not make use of any commercial consultants concerning graduation. A third party did not receive any nonmonetary perquisites, neither directly nor indirectly, for activities that are connected with the contents of the presented thesis. All sources of information are clearly marked, including my own publications.

In particular, I have not consciously:

Fabricated data or rejected undesired results

Misused statistical methods with the aim of drawing other conclusions than those warranted by the available data

Plagiarized data or publications

Presented the results of other researchers in a distorted way

Presented AI-generated content (graphs, text, code, or data) beyond the aforementioned grammar correction.

I do know that violations of copyright may lead to injunctions and damage claims of the author, and also to prosecution by the

law enforcement authorities.

I hereby agree that the thesis may need to be reviewed with an electronic data processing for plagiarism.

This work has not yet been submitted as a doctoral thesis in the same or a similar form in Germany or in any other country. It has not yet been published as a whole.

Magdeburg, May 27, 2025